The impact of marine growth on submerged power cables

Anja Slim[1] Edward Hinton[2] Graeme Hocking[3]
Sami Al-Izzi[4] Nitay Ben-Shachar[5] Phil Broadbridge[6]
Pierluigi Cesana[7] Michael Dallaston[8] Daniel Hayes[9]
Edoardo Fabbrini[10] Chathranee Jayathilake[11]
Benjamin Lee[12] Melanie Roberts[13] Cal Robertson[14]
Jia Jia Qian[15] Sergey Suslov[16] Rahil Valani[17]
Liam Yemm[18] Wu Yunpei[19]

Sun Cable Representatives:

Joe Bunton, Mark Nuttall, Jakub Tomczyk

DOI:10.21914/anziamproc.v65.19271, © Austral. Mathematical Soc. 2026. Published 2026-10-27, as part of the Proceedings of Mathematics in Industry Study Group, 2023. ISSN 1445-8810. (Print two pages per sheet of paper.) Copies of this article must not be made otherwise available on the internet; instead link directly to the DOI for this article.

Abstract

As part of the MISG in 2023 at Monash University, Sun Cable posed several questions related to the bio-fouling of submarine transmission cables for their installation between Darwin and Singapore. The Coral Triangle has a great bio-diversity and a range of different seabed and physical conditions, leading to highly variable conditions. The group considered growth factors, hydrodynamic effects, and heating and insulation impact on the hanging or buried cables across the range of different conditions over the proposed path.

Study Group Participants:

Sami Al-Izzi, Nitay Ben-Shachar, Phil Broadbridge, Pierluigi Cesana, Michael Dallaston, Edoardo Fabbrini, Daniel Hayes, Edward Hinton, Graeme Hocking, Chathranee Jayathilake, Benjamin Lee, Melanie Roberts, Cal Robertson, Jia Jia Qian, Anja Slim, Sergey Suslov, Rahil Valani, Liam Yemm, Wu Yunpei.

Contents

1 Introduction **M46**

2 Potential for marine growth **M47**

3 Thermal performance **M49**
3.1 Introduction . . . M49
3.2 Literature review . . . M49
3.3 Study group overview . . . M51
3.4 Problem formulation . . . M52
3.4.1 Cable configuration . . . M53
3.4.2 Governing equations within the cable . . . M53
3.4.3 Equations in the conducting core . . . M54
3.4.4 Equations in the insulating layers . . . M56
3.4.5 Interfacial conditions between layers . . . M56
3.4.6 Outside the cable . . . M57
3.4.7 Convective cooling by seawater . . . M57
3.4.8 Marine growth . . . M58
3.4.9 Sediment . . . M59
3.5 Temperature profile for a clean, exposed cable . . . M59
3.5.1 Solution in the insulating layers . . . M59
3.5.2 A single effective conductivity . . . M60
3.6 Solution for the core temperature . . . M60
3.6.1 Results for clean cable . . . M61
3.6.2 Adding a marine growth layer: The worst-case scenario M61
3.6.3 Results of added marine growth layer . . . M66
3.7 A random, conduction-only marine-growth layer . . . M66
3.8 Results . . . M69
3.9 A buried cable . . . M70
3.9.1 Results . . . M72
3.10 Summary and discussion . . . M73

4 Hydrodynamics **M75**

4.1 Background M76
4.2 Laminar flow past a cylinder M77
4.3 Unsteady flow M80
4.4 Computational Fluid Dynamics Modelling M81
4.5 Vortex-induced vibration M85
4.6 Mathematical model M86
4.7 Sample calculations of vortex induced oscillations M89

5 Summary M89

A Thermal performance appendices M90

B Value of the heat transfer coefficient M90

C An alternative solution method for §§3.5.1 M91

D Temperature distribution in a conducting core M92

E MATLAB code for maximum cable temperature M96

F MATLAB code for the thickness of marine growth M100

G An exact solution to a non-axisymmetric problem M105

H Further exploration of Chapter 3 M107

1 Introduction

The company Sun Cable intends to install a cable to transmit power generated in the Northern Territory to Singapore. The proposed route of the Darwin-Singapore *PowerLink* passes through the Coral Triangle, a global centre of marine biodiversity. The cable will be approximately 4200 km in length and will be installed at depths of up to 1924 m below sea level.

Sun Cable posed a series of questions that relate to the performance of their proposed power cable over this route, and specifically the effects of marine growth on the cable:

1. What substances in water and what water parameters contribute to marine growth?
2. What is the relationship between marine growth and water depth?
3. What effect does marine growth have on steady state thermal performance of subsea cables? How does it compare to soil?
4. What effect does marine growth have on hydrodynamic forces acting on subsea cables?

We address the four questions posed by Sun Cable above in the following sections. Firstly, there is a general examination of the potential for marine growth on the cables, followed by the implications of growth on the cable for heat build up and hence deterioration in performance. Hydrodynamic effects are considered in the next section, including flow past the cables on or off the bed and including lift and drag calculations and oscillations due to vortex generation. We note that there are existing reports on the behaviour of high voltage direct current (HVDC) links such as the report on the Basslink in Australia between Victoria and Tasmania (Sherwood *et al.*, 2016) that provide additional valuable observational information.

2 Potential for marine growth

The first questions posed by Sun Cable concerned the distribution of marine growth and how this relates to depth and seawater composition and other water parameters, and how this might impact on the cable.

Biofouling is a significant challenge faced by various maritime industries that employ submerged structures. If not addressed adequately, it can result in increased costs and reduced operational lifespans. In extreme cases it may directly damage the cable. For example, Scott (1991) describes the failure of PVC piping owing to bivalves that bore into the solid over a relatively short period of time. Effective management of biofouling requires insight into the ongoing processes at the relevant marine locations. However, information on composition and magnitude of biofouling is often scattered across different sources, which can make studying it time-consuming.

Marine growth can be divided into two categories: vegetable (e.g., algae) and animal (e.g., mussel, anemones, and corals). The growth can quickly cover structures, hindering visual inspections, increasing cleaning costs for oil industries, and increasing hydrodynamic forces on the structure.

For the marine renewable energy (MRE) sector, this issue poses a particular concern. Vinagre *et al.* (2020) developed a European biofouling database to support the MRE sector and other maritime industries. The database compiles qualitative and quantitative data on challenging biofouling groups, including non-native species associated with MRE and related marine equipment in different European eco-regions. It provides information on the occurrence of fouling species and key biofouling parameters such as thickness and weight. The database aims to facilitate informed decisions by helping the MRE sector and offshore industries understand the biofouling communities to which their devices are most susceptible at a given site. However this information is based on data for European seas, and extrapolation to the Indonesian seas should be approached with caution.

According to Vinagre *et al.* (2020), *"predicting and modeling biofouling compo-*

sition and magnitude can be a daunting task, especially with the differences in biofouling communities at different geographic locations and biotopes". Limited statistical models exist linking the extent of growth with depth, seawater temperature and other ocean conditions, but the majority of these are based on North Sea and European waters (Forteath *et al.*, 1982).

The study presented by Schoefs & Ameryoun (2013) aims to probabilistically model marine growth colonisation in the Gulf of Guinea and its effect on quasi-static behaviour of jacket type offshore structures and may be more directly relevant to Indonesia. Further studies with detailed and statistically robust analyses of biofouling in the Indonesian seas and its impacts are needed to provide more location-specific information on the possible extent of biofouling of the proposed cable.

In general, the thickness of marine growth on structures may range from a few centimetres up to 20–30 cm at water depths of up to 100 m, with reduced growth below 200 m where photosynthesis ceases. Light and temperature are the major limiting factors on growth, and so at greater depths there is much less potential for biofouling as light diminishes and temperature decreases.

Indonesia has great strategic potential for marine renewable energy, not only to achieve its renewable energy goals, but also to ensure access to clean energy across the archipelago. Despite being in the early phase of development, marine energy in Indonesia has seen an emphasis on resource assessment and prototype testing of power generation technologies. However, specific research on the effects of biofouling on the durability of marine energy infrastructure in Indonesia is lacking, according to available literature. Iswadi *et al.* (2022) develop a matrix to identify and predict key fouling organisms and their possible risks on marine renewable energy infrastructure in tropical waters of Indonesia. This matrix is based on the analysis of previous findings in temperate and subtropical waters. The matrix identifies calcareous polychaetes (*Serpulidae* - tubeworms), barnacles (*Amphibalanus spp.*), and bivalves (*Perna viridis* - green mussels) as some possible key fouling organisms that may pose risks to marine energy infrastructure in Indonesia

by increasing weight and drag and causing corrosion.

3 Thermal performance

3.1 Introduction

Subsea power cables are typically composed of several concentric layers, with the innermost one an electrical conductor. Electrical current through this conducting core generates heat, which conducts through the surrounding electrical insulators and into the environment. The question posed by Sun Cable was whether marine growth could provide sufficient additional insulation to cause temperatures within the insulating layers to exceed the maximum operating temperature. The insulating layers currently have a specified maximum allowable operating temperature of around 70 °C; future cables are anticipated to be rated to 80–90 °C.

3.2 Literature review

The following is a brief review of some relevant literature that illustrates the range of issues that have been considered previously. It should not be considered an exhaustive summary. There are a number of applications in which undersea cables are utilised, and the experiences from those systems can be instructive in the current problem.

The use of submarine high-voltage (HV) cables is necessary for the expansion of offshore renewable energy infrastructure and the need for trans-continental shelf power transmission. These cables can operate at temperatures up to 70°Cand are typically buried 1–2 m beneath the seabed in a variety of substrates found on the continental shelf. However, little is known about the heat flow pattern and potential effects on sedimentary environments around such high heat sources near the surface sediments.

Čiegis *et al.* (2007) presented a set of mathematical models and numerical algorithms for the heat transfer problem in cable bundles that, although

different to the design specifications here, are informative in raising the important thermal issues. The numerical algorithms are targeted to the two-dimensional transient heat transfer problem. Results of numerical experiments are presented. In a study presented by Emeana *et al.* (2016), temperature measurements from a 2-D laboratory experiment were used to identify the thermal regimes generated within typical unconsolidated shelf sediments, including coarse silt, fine sand, and very coarse sand. The experiment used a large tank filled with water-saturated spherical glass beads (ballotini) and instrumented with a buried heat source and 120 thermocouples to measure the evolving temperature distributions. The steady-state heat flow regimes and normalised radial temperature distributions were assessed through the experimental observations and corresponding Finite Element Method simulations. Results indicated that heat transfer and temperature fields generated from submarine HV cables buried within a range of sediments can be highly variable. Coarse silts are shown to be purely conductive, producing temperature increases of over 10°C up to 40 cm from a source at 60°C above ambient. Fine sands demonstrate a transition from conductive to convective heat transfer for sources between 20 and 36°C above ambient, with heat increases of over 10°C occurring over a metre from the source when at 55°C above ambient. Very coarse sands are dominated by convective heat transfer even at very low operating temperatures, reaching temperatures of up to 18°C above ambient at a metre from the source. The transition from predominantly conductive to predominantly convective heat transfer was shown to occur at a permeability of $10^{-11}\,m^2$ for excess temperatures of 30 °C and above, and higher permeabilities for lower excess temperatures. These findings are essential for understanding the surrounding near-surface environments that experience such high temperatures and may have significant implications for chemical and physical processes at the grain and sub-grain scales, biological activity at both micro-faunal and macro-faunal levels, and the operational performance of the cables themselves. Convective heat transport would increase cable current ratings, something that is not considered in existing standards.

Around exposed cables, biofouling can alter heat transfer, affecting the max-

imum conductor temperature, as well as induce temperature fluctuations, which can influence the lifetime of the cable due to wear and fatigue. The study presented by Maksassi *et al.* (2022) measured the effective thermal conductivity of a layer of mussels of various ages and the effective heat transfer coefficient between the layer and the surrounding water. The findings indicate that the effective thermal conductivity of juvenile mussels is lower than that of mixed and adult mussels. This variability in effective thermal conductivity with mussel age is related to the porosity of the mussel layer. The effective heat transfer coefficient is significantly higher than for a smooth surface. This effect may be surprising at first glance. However it is known that increased surface roughness can cause increased heat transfer (e.g., Tummers & Steunebrink, 2019). Using the measured parameters, the authors numerically simulated the effect of a layer of mussels on the thermal performance of a cable. They suggest that biofouling could lead to insulating effects for cables colonised by juvenile or mixed mussels, but could potentially cause cooling if colonised by adult mussels.

3.3 Study group overview

Keeping this literature in mind, the study group considered several questions related to heat transfer. We first considered the worst-case scenario: a uniformly thick layer of growth in which heat is only transferred by conduction. Specifically, we calculated how thick the marine layer would need to be for the maximum operating temperature to be exceeded, depending on the electrical current, the specifications of the cable, the seawater temperature and the thermal conductivity of the marine growth. This calculation included the effect of temperature on electrical resistivity. As an extension of this problem, we also numerically calculated the temperature distribution in the cable with a marine growth layer of random thickness.

Finally, for comparison purposes, we considered the case of a cable buried to a given depth in sediment. Here we were able to provide a simple analytic solution for a conductor-only cable. Extensions to multi-layer cables are

possible although more involved; such solvers appear to be available already. These were not considered by the group.

3.4 Problem formulation

We consider heat flow through a cylindrical cable with an axisymmetric internal geometry. Heat is generated in the inner electrically conducting core of the cable through Joule heating. This heat conducts through the surrounding insulating layers of the cable before being transported by conduction or convection through a variety of external media.

List of symbols

c_p is the specific heat coefficient ($\mathrm{J\,K^{-1}\,kg^{-1}}$)

k_i is the thermal conductivity of layer i ($\mathrm{W\,K^{-1}\,m^{-1}}$)

k_f is the thermal conductivity of layer of any marine growth ($\mathrm{W\,K^{-1}\,m^{-1}}$)

$q(T)$ is the rate of heat generation in the conducting core per unit volume ($\mathrm{W\,m^{-3}}$)

$Q(T)$ is the rate of heat generation per unit length of the cable ($\mathrm{W\,m^{-1}}$)

r_i is the outer edge of layer i (m)

r_1 is the radius of the conducting core

$R(T)$ is the electrical resistance of the conducting core per unit length ($\Omega\,\mathrm{m^{-1}}$)

R_{ref} is the resistance per unit length at a reference temperature T_{ref} ($\Omega\,\mathrm{m^{-1}}$)

T is the temperature (°C)

T_i is the temperature at $r = r_i$

T_1 is the temperature at $r = r_1$, the edge of the conducting core

T_{ref} is the temperature at which the thermal conductivity of copper is measured

T_{sea} is the sea temperature

α is the heat transfer coefficient ($W\,K^{-1}\,m^{-2}$)

β is the increase in R per unit temperature, $dR/dT|_{T=T_{ref}}$ ($\Omega\,K^{-1}\ m^{-1}$)

$\kappa_i = k_i/(\rho c_p)$ is the diffusivity of layer i ($m^2\,s^{-1}$)

ρ is the mass density ($kg\,m^{-3}$)

3.4.1 Cable configuration

The cable geometry is described by cylindrical polar coordinates with r the radial coordinate and z the along-cable coordinate. The inner conductive core has radius r_1 and thermal conductivity k_1. It is surrounded by $n-1$ uniform thickness, coaxial, electrically (and thermally) insulating layers. Layer i extends from r_{i-1} at its inner edge to r_i at its outer edge and has thermal conductivity k_i. This configuration is illustrated in Fig. 1.

Our analysis is general to any axisymmetric cable. However, to provide illustrative results, we also specifically consider the cable geometry provided by Sun Cable and illustrated in Fig. 2. This cable comprises an inner copper core of radius 30 mm and a further nine electrically insulating layers of varying thicknesses and thermal properties. The total cable radius is 81 mm.

3.4.2 Governing equations within the cable

Within the cable, we treat the problem as a steady-state heat conduction problem with electrically induced heating in the conductive core. Steady state is relatively quickly reached. The time-scale for heat diffusion, L^2/κ, is of the order of a day over the radius of the cable and is weeks to months for a layer of 1 m or more of sediment. This is significantly shorter than the expected

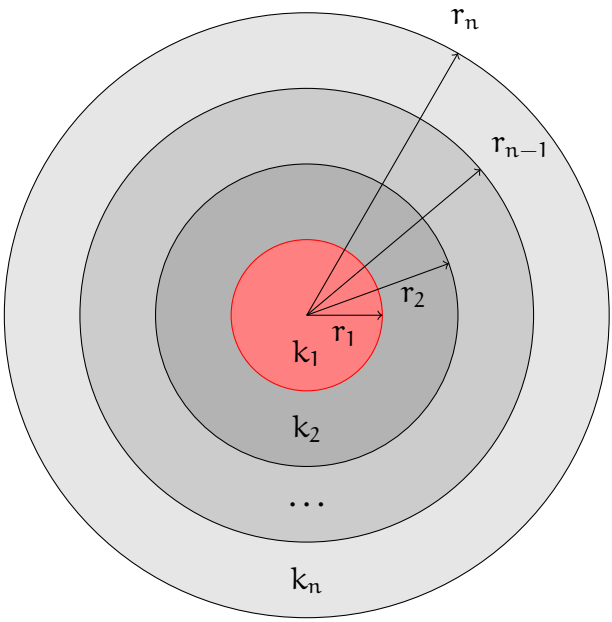


Figure 1: Generic axisymmetric cable geometry and related notation. The electrically conducting core is highlighted in red. The remaining $n-1$ layers are electrical insulators.

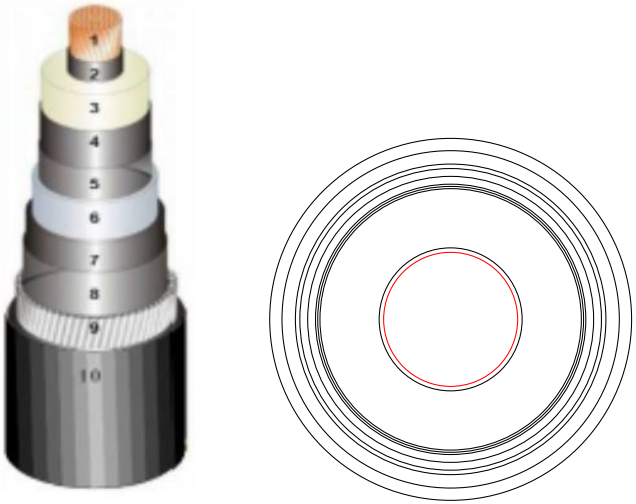
lifespan of the cable. Steady state is also the worst-case scenario as far as the temperatures that develop in the cable and hence is an appropriate limit for the question under consideration.

We also ignore thermal diffusion in z (along-cable diffusion). This is reasonable as changes along the cable occur on a much longer scale than the centimetre to metre scale of the cross-cable variations.

3.4.3 Equations in the conducting core

In the conducting core the temperature T obeys

$$0 = k_1 \nabla^2 T + q,$$



i	1	2	3	4	5	6	7	8	9	10
r_i, mm	30	32	58.5	59.5	60.5	64	67.5	69.5	75.5	81
k_i, W/(m·K)	395	1	0.285	1	1	60	0.4	0.11	50	0.11

Figure 2: Specific example: cable geometry (top left) and cable cross-section (top right) showing the 10 layers to scale. The inner core is shown in orange/red, and the nine layers that make up the insulation are in grey/black. The radii and thermal conductivities of the layers are given in the table.

where ∇^2 is the two-dimensional Laplacian, independent of z, and q is the rate of heat generation per unit volume.

Heat is generated by the electrical current flowing through the core and we need to connect q with the current, the electrical properties of the material and the temperature. A detailed discussion of q and a full calculation for the temperature in the cable allowing for its spatial variability within the core is given in Appendix D.

Here we assume that, because of its high thermal conductivity, the temperature in the core is nearly constant and can be approximated well by the temperature at its edge, $T(r_1) = T_1$. In our results, we show that this is a very reasonable approximation. Under this assumption, q is uniform across the core and the total heat generated per unit length of the cable is $Q(T_1, I) = \pi r_1^2 q$ for an electrical current I. This total heat generation is related to the current through the relationship

$$Q(T_1, I) = I^2 R(T_1), \tag{1}$$

where R is the electrical resistance of the core per unit length. We approximate the resistance as either constant

$$R(T) = R_r \tag{2}$$

or as linearly dependent on temperature,

$$R(T) = R_r + \beta(T - T_r), \tag{3}$$

where R_{ref} is the resistance per unit length at a given reference temperature T_{ref} and $\beta = dR/dT|_{T=T_{ref}}$ is the increase in resistance per unit temperature.

3.4.4 Equations in the insulating layers

The temperature distribution in each insulating layer is described by the steady state heat equation but now without a source, which reduces to Laplace's equation

$$\nabla^2 T = 0, \qquad i = 2, \ldots, n. \tag{4}$$

3.4.5 Interfacial conditions between layers

At $r = r_i$, the interface between layer i and layer $i+1$, we impose continuity of temperature and continuity of heat flux,

$$T \text{ continuous at } r = r_i \quad k_i \left.\frac{dT}{dr}\right|_{r=r_i^-} = k_{i+1} \left.\frac{dT}{dr}\right|_{r=r_i^+}. \quad i = 1, \ldots, n-1. \tag{5}$$

At the edge of the core, the latter condition can be replaced by

$$k_1 \left.\frac{dT}{dr}\right|_{r=r_1^-} = -\frac{Q}{2\pi r_1} = k_2 \left.\frac{dT_2}{dr}\right|_{r=r_1^+} . \tag{6}$$

3.4.6 Outside the cable

Outside the cable, we consider three different environments:

1. immediate contact with seawater, which provides convective cooling;
2. a marine growth layer in which heat is transported by conduction (as the worst case scenario) and which in turn is surrounded by seawater; and
3. a sediment layer in which heat is transported only by conduction and that extends up to a horizontal seafloor.

3.4.7 Convective cooling by seawater

The seawater temperature along the path of the cable is shown in Fig. 3. In shallow portions it is a relatively uniform 30°C while in deeper portions it is a relatively uniform 5°C. These values are not expected to vary greatly during the year.

We assume that at any interface with seawater, the heat flux obeys Newton's law of cooling

$$k_n \boldsymbol{\nabla} T \cdot \mathbf{n} = \alpha (T_{sea} - T) , \tag{7}$$

where $\mathbf{n}$ is the normal to the interface, α is the convective heat transfer coefficient and T_{sea} is the seawater temperature. We take the value $\alpha = 200\,\mathrm{W\,K^{-1}\,m^{-2}}$ following Maksassi *et al.* (2022), based on their experimental values for a clean metal cylinder. This is likely to be an underestimate for the true value, although the results presented are not sensitive to the precise value. In fact, the range of reasonable values of α are sufficiently high that

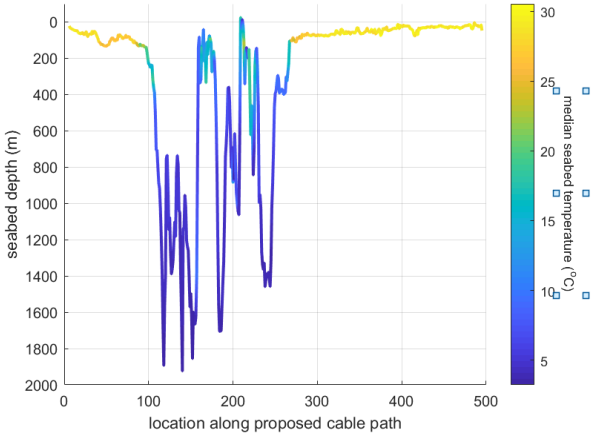


Figure 3: Properties along the length of the cable: seafloor depth (curve) and average seawater temperature on the seafloor (colour).

this condition can be well-approximated by $T = T_{sea}$. A further discussion of the value of α is given in Appendix B.

3.4.8 Marine growth

As described in section 2, marine growth could take a variety of forms. We focus on the case where the growth is assumed to be sufficiently dense that heat transfer occurs only by conduction. This is unlikely to be accurate, but again provides an upper bound for the temperatures that develop in the cable. With this assumption, heat transfer in the marine-growth layer is also modelled according to (4). In the case that the marine growth is primarily soft-bodied, the conductivity of the layer k_f can be approximated by that of water, $k_f = 0.6\,\mathrm{W\,K^{-1}\,m^{-1}}$. For mussels, measured values of effective conductivity range from 4.4 to $12.8\,\mathrm{W\,K^{-1}\,m^{-1}}$ (Maksassi *et al.*, 2022), although these measurements incorporated some convective effects. Note that the conductivity of water provides a lower bound for the conductivity of the marine-growth layer and hence using this value gives an upper bound

on the temperatures that can develop.

3.4.9 Sediment

Finally, for comparison purposes we also briefly consider a cable buried in a static homogeneous sediment. We model heat transfer by conduction, thus (4) is again valid in this layer. An effective heat transfer coefficient in the sediment is denoted k_{sediment}.

3.5 Temperature profile for a clean, exposed cable

We begin by considering a clean cable without any marine growth and surrounded by seawater and obtain solutions for different scenarios. These general solutions can be extended to consider the various different cases.

3.5.1 Solution in the insulating layers

The temperature profile within the insulating layers can be obtained by solving the Laplace's equation for the temperature profile in (4). An alternative, more compact approach based on Fourier's law is given in Appendix C.

In this scenario, the temperature is axisymmetric and the Laplacian $\nabla^2 T$ in (4) becomes

$$\nabla^2 T = \frac{1}{r}\frac{d}{dr}\left(r\frac{dT}{dr}\right).$$

The general solution of (4) for $r_{i-1} \leqslant r \leqslant r_i$ is then

$$T = A_i + B_i \log\frac{r}{r_{i-1}}, \quad i = 2, 3, \ldots, n \tag{8}$$

with

$$A_i = T_1 - \frac{Q}{2\pi}\sum_{j=2}^{i-1}\frac{1}{k_j}\log\frac{r_j}{r_{j-1}}, \quad B_i = -\frac{Q}{2\pi k_i}, \tag{9}$$

for the particular solution with boundary conditions (5) and (6). Here $T_1 = T(r_1)$ and is the maximum temperature in the insulating layers of the cable.

Substituting this form into the outer boundary condition (7) imposed on $r = r_n$, we finally obtain the relation

$$T_1 = T_{sea} + \frac{Q}{2\pi}\frac{1}{k_e}, \tag{10}$$

where k_e is an effective conductivity

$$\frac{1}{k_e} = \sum_{i=2}^{n} \frac{1}{k_i} \log\left(\frac{r_i}{r_{i-1}}\right) + \frac{1}{\alpha r_n}. \tag{11}$$

3.5.2 A single effective conductivity

This expression also allows us to approximate the multi-layer insulation from our illustrative cable by a single layer with a conductivity k_{single} given by

$$\frac{1}{k_{single}} = \sum_{i=2}^{n} \frac{1}{k_i} \log\left(\frac{r_i}{r_{i-1}}\right) \approx 0.3\,\mathrm{W\,K^{-1}\,m^{-1}} \tag{12}$$

extending from a radius of 30 mm to 81 mm.

3.6 Solution for the core temperature

The full derivation of the core temperature distribution is given in Appendix D. Here we assume the temperature is constant in the core and use (1) to calculate Q. This provides an accurate approximation as we observe in the results below.

Combining (1) and (10), an implicit equation for the temperature difference between the core and the sea water is then

$$T_1 - T_{sea} = \frac{I^2[R_{ref} + \beta(T_1 - T_{sea}) + \beta(T_{sea} - T_{ref})]}{2\pi k_e}. \tag{13}$$

Solving for the temperature drop $T_1 - T_{sea}$ then gives

$$T_1 = T_{sea} + \frac{I^2[R_{ref} + \beta(T_{sea} - T_{ref})]}{2\pi k_e - I^2\beta}. \tag{14}$$

3.6.1 Results for clean cable

Fig. 4 shows the temperature profile in the cable for the illustrative geometry given in Fig. 2 using the full derivation for the core from Appendix D. The temperature in the core is indeed nearly constant.

Fig. 5 shows how the maximum temperature in the insulating layers, equivalently the temperature at the core-insulation boundary T_1, varies with the electrical current flowing through the cable. For a maximum operating temperature of 70°C, the largest permitted current is around 3100 A in shallow water at 30°C and around 3900 A in deep water at 5°C. Note that the increase in electrical resistance with core temperature is an important effect to include, increasing the predicted temperature differences from ambient by around 10%. The code for the plot is provided in Appendix E.

3.6.2 Adding a marine growth layer: The worst-case scenario

The worst-case scenario for marine growth from a thermal performance perspective is a uniform layer in which only conductive heat transfer occurs. Here we calculate the maximum allowed thickness for this layer for the cable to remain within operating bounds.

Let Δr_f be the thickness of the marine growth layer and let its thermal conductivity be k_f. This layer simply behaves as an additional axisymmetric layer of insulation. The calculations of the previous section remain valid with an effective conductivity $k_{e,f}$ now given by

$$\frac{1}{k_{e,f}} = \sum_{i=2}^{n} \frac{1}{k_i} \log(r_i/r_{i-1}) + \frac{1}{k_f} \log(1 + \Delta r_f/r_n) + \frac{1}{(r_n + \Delta r_f)\alpha}. \tag{15}$$

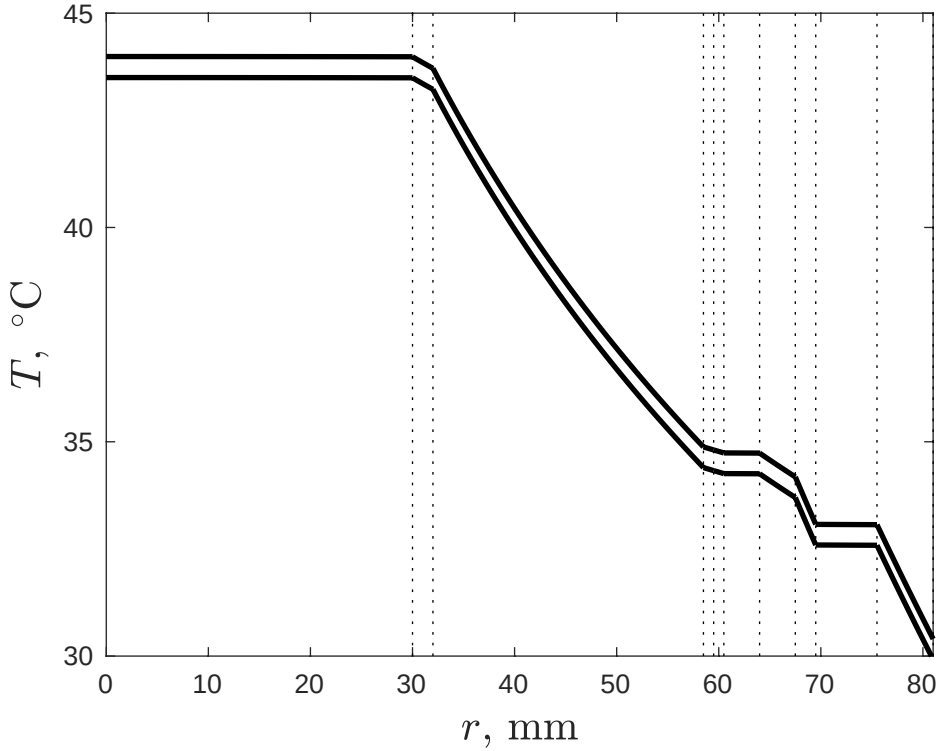
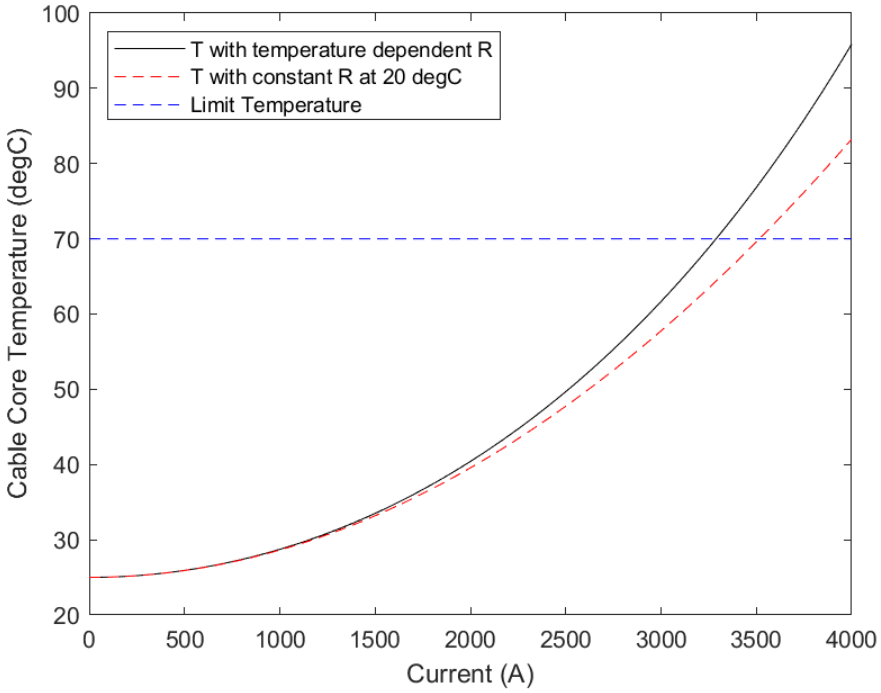
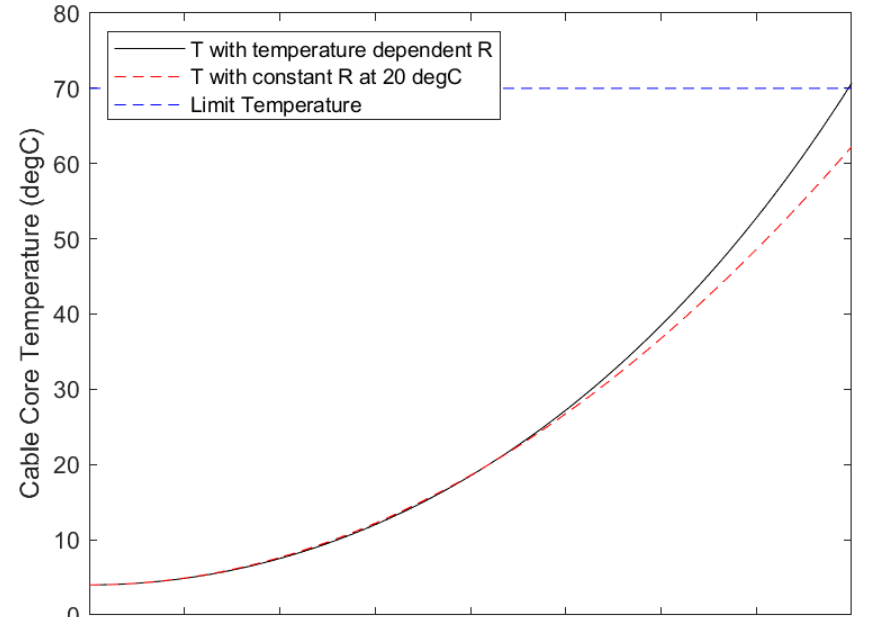


Figure 4: The temperature distribution in a clean cable with properties given in Fig. 2 carrying electric current $\mathrm{I} = 2000\,\mathrm{A}$ and surrounded by seawater with temperature $\mathsf{T}_{\mathrm{sea}} = 30°\mathrm{C}$. The heat transfer coefficients are $100\,\mathrm{W\,K^{-1}\,m^{-2}}$ (top curve) and $2000\,\mathrm{W\,K^{-1}\,m^{-2}}$ (bottom curve). This plot is based on the full calculation given in Appendix D.


T with temperature dependent R
T with constant R at 20 degC
Limit Temperature
Cable Core Temperature (degC)
Current (A)
100
90
80
70
60
50
40
30
20
0
500
1000
1500
2000
2500
3000
3500
4000


T with temperature dependent R
T with constant R at 20 degC
Limit Temperature
Cable Core Temperature (degC)
80
70
60
50
40
30
20
10

Let T_{max} be the maximum allowable operating temperature. Substituting (15) into (10), an implicit equation for the thickness of the marine growth layer resulting in the core/insulator boundary having a temperature of $T_1 = T_{max}$ is obtained:

$$T_{max} - T_{sea} = \frac{Q(T_{max}, I)}{2\pi} \left(\sum_{i=2}^{n} \frac{\log(r_i/r_{i-1})}{k_i} + \frac{\log(1 + \Delta r_f/r_n)}{k_f} + \frac{1}{(r_n + \Delta r_f)\alpha} \right). \tag{16}$$

This can be solved for Δr_f using a standard root finding algorithm, such as `fzero` in MATLAB.

If the thermal resistance due to convection is small compared to the combined thermal resistance to conduction,

$$\frac{1}{r_n \alpha} \ll \sum_{i=2}^{n} \frac{\log(r_i/r_{i-1})}{k_i}, \tag{17}$$

then the effective conductivity may be approximated as

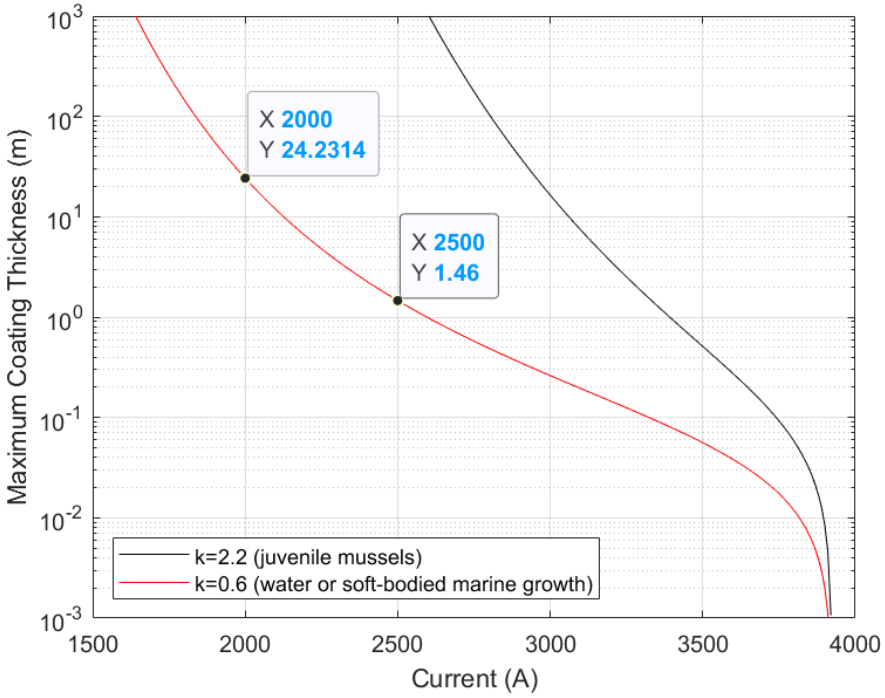
$$\frac{1}{k_{e,f}} \approx \frac{1}{k_e} + \frac{\log(1 + \Delta r_f/r_n)}{k_f}. \tag{18}$$

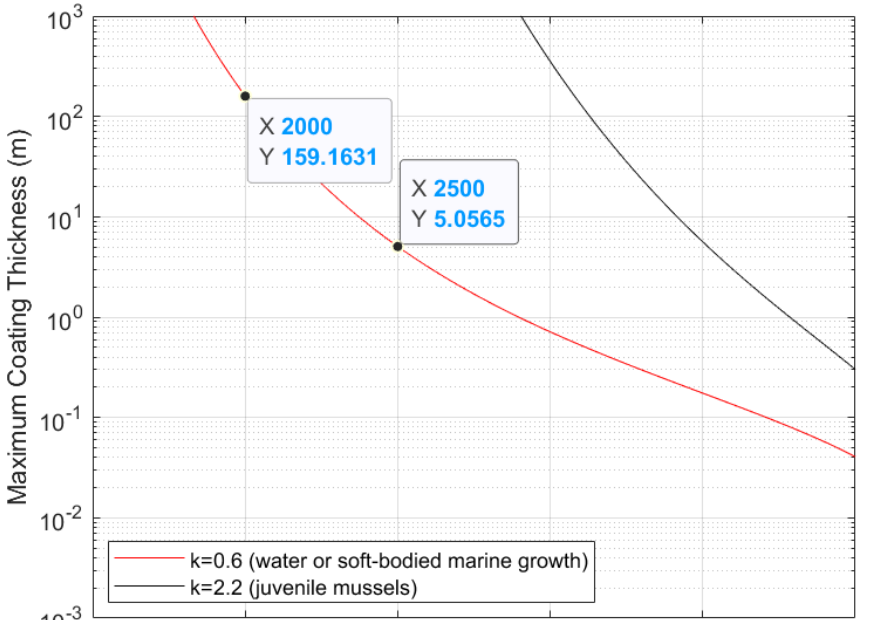
Substituting (18) into (10) now gives

$$T_{max} - T_{sea} = \frac{Q(T_{max}, I)}{2\pi} \left(\frac{1}{k_e} + \frac{\log(1 + \Delta r_f/r_n)}{k_f} \right). \tag{19}$$

Solving this equation for Δr_f gives a closed-form solution for the maximum allowable marine thickness,

$$\Delta r_f = r_n \left[\exp\left(k_f \left[\frac{2\pi(T_{max} - T_{sea})}{Q(T_{max}, I)} - \frac{1}{k_e} \right] \right) - 1 \right] \tag{20}$$


X 2000
Y 24.2314
X 2500
Y 1.46
k=2.2 (juvenile mussels)
k=0.6 (water or soft-bodied marine growth)
Maximum Coating Thickness (m)
Current (A)
10^3
10^2
10^1
10^0
10^-1
10^-2
10^-3
1500
2000
2500
3000
3500
4000


X 2000
Y 159.1631
X 2500
Y 5.0565
k=0.6 (water or soft-bodied marine growth)
k=2.2 (juvenile mussels)
Maximum Coating Thickness (m)
10^3
10^2
10^1
10^0
10^-1
10^-2

3.6.3 Results of added marine growth layer

Fig. 6 shows the maximum coating thickness as a function of the electrical current in the cable for different kinds of marine growth. Considering a significant marine growth layer of 1 m thickness, a cable in deep water with a maximum operating temperature of 70 °C could safely operate with currents up to approximately 2600 A and a cable with a maximum operating temperature of 90 °C could safely operate with currents up to approximately 2800 A.

The code for the plot is provided in Appendix F. The solutions shown are for (16), but those using (20) are indistinguishable on the scale shown.

3.7 A random, conduction-only marine-growth layer

A computational method is used to examine the effect of a random marine growth layer in which heat is only transferred by conduction. In particular, we will compare a clean cable with no marine growth to a series of domains having an increasing amount of random growth around the cable. In contrast to the previous section in which the shape was assumed to be axi-symmetric, the solution will be obtained for a randomly shaped growth, as might be encountered in the ocean.

To reduce the computational complexity, we approximate the nine insulating layers in the example geometry by a single layer with an effective conductivity given by (12). We assume the marine layer has a conductivity of $k_f = 0.6\,\mathrm{W\,K^{-1}\,m^{-1}}$. The condition $T = T_{sea}$ is applied on the outer edge of the marine growth layer, although applying (7) does not produce significantly different results.

Here we rescale the variables as follows

$$\mathbf{x} = r_n \mathbf{x}^*, \quad T = T_{sea} + \frac{q r_n^2}{k_1}\,\theta^*, \tag{21}$$

where $\mathbf{x}^*$ represents the dimensionless coordinates and θ^* is a dimensionless temperature difference. We write the governing equations with these rescalings

as

$$\boldsymbol{\nabla}^* \cdot (k^* \boldsymbol{\nabla}^* \theta^*) = -q^* \quad \text{in } \Omega \tag{22}$$

$$\theta^* = 0 \quad \text{on } \partial\Omega, \tag{23}$$

where Ω is the full computational domain. The dimensionless heat source q^* is piece-wise constant and takes the value 1 in the core and 0 outside the core. The dimensionless conductivity is also piece-wise constant and is given by

$$k^*(x, y) = \begin{cases} 1 & \text{if} \quad r^* < r_1/r_n \\ k_{\text{single}}/k_1 = 10^{-3} & \text{if} \quad r_1/r_n \leqslant r^* < 1\,. \\ k_f/k_1 = 2 \times 10^{-3} & \text{otherwise} \end{cases} \tag{24}$$

The different values of the conductivity correspond to the values in the cable core, the insulator and the marine growth layer. This assumes a conductivity of $k_1 = 300\,\mathrm{W\,K^{-1}\,m^{-1}}$ in the inner core, which is slightly lower than the value in the illustrative example of Fig. 2.

This problem is solved numerically via the hybrid high-order method (Di Pietro & Droniou, 2020). Hybrid high-order (HHO) schemes are modern polytopal methods for the approximation of elliptic PDEs. A key aspect of HHO is its applicability to generic meshes with arbitrarily shaped polytopal elements. Moreover, HHO methods are of arbitrary order, and are cheap to implement due to the compact global stencil achieved via static condensation of the element unknowns. However, the particular problem considered here requires a mesh with curved edges due to the curved boundary, and discontinuities in the diffusion coefficient along circular arcs. We follow the approach taken by Yemm (2023*a*) to defining unknowns on curved edges and designing numerical quadrature rules on elements with curved edges.

We implement here a HHO scheme to solve problem (22)–(24) on various domains using the open source C++ library `PolyMesh` (Yemm, 2023*b*). We take a background Cartesian mesh with 16 384 elements, and 'cut-out' the domain of interest. The random growth on the domain is achieved by cutting

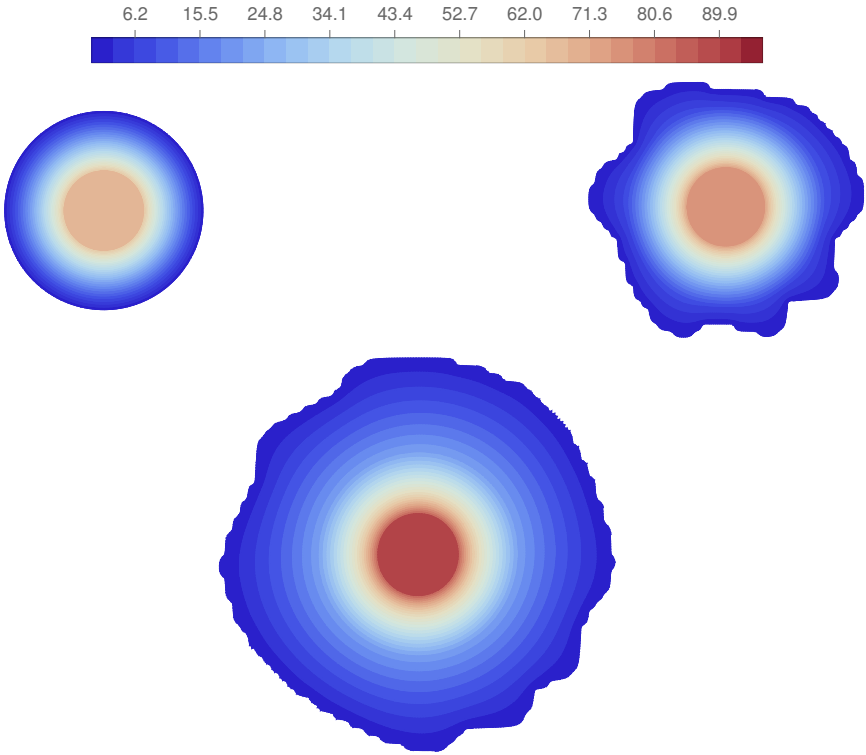


Figure 7: Dimensionless temperature profiles θ^* with varying levels of marine growth. The top left cable is clean.

along an increasingly large, but very rough curve. We consider an HHO method of degree 2, which corresponds to a degree 3 approximation (a cubic polynomial on each mesh element).

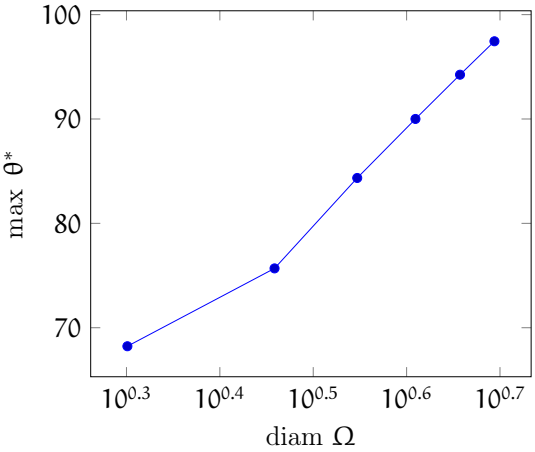


Figure 8: Maximum dimensionless temperature versus maximum domain diameter.

3.8 Results

In Fig. 7, we plot the dimensionless temperature profiles on various domains with an increasing amount of marine growth. Dimensional temperatures can be obtained from these values by solving the implicit equation

$$T_1 = T_{sea} + \frac{Q(T_1, I) r_n^2}{\pi r_1^2 k_1} \theta_1^*$$

for T_1 with Q given by (1). Here $\theta_1^* = \max_{r^*=r_1/r_n} \theta^*(r^*)$ is the maximum dimensionless temperature at the edge of the core. With T_1 known from this equation, we can find the value of $q = Q(T_1, I)/\pi r_n^2$ required to redimensionalise the temperature profiles according to (21).

In Fig. 8, we plot the dimensionless maximum temperature achieved in the cable core against the maximum diameter of the domain on a log-linear axis.

3.9 A buried cable

For a final comparison, we consider a cable buried in a homogeneous, static sediment in which heat transfer is only by conduction. Commercial code exists for this problem for detailed geometries such as that given in Fig. 2. Here we only provide a useful analytic solution for the simplified case where the sediment and insulating layers have the same conductivity.

Here we model the steady heat-conduction problem from a core of radius r_1 buried to a depth h in a semi-infinite sediment in $y < 0$. The core is at uniform temperature T_1 as a result of its much higher thermal conductivity. The equation for this problem is

$$\nabla^2 T = 0$$

in the domain $x^2 + (y + h + r_1)^2 > r_1^2$ and $y < 0$ with boundary conditions $T = T_1$ on $x^2 + (y + h + r_1)^2 = r_1^2$ and $T = T_{sea}$ on $y = 0$.

We rescale this problem slightly differently from §3.7, setting

$$\mathbf{x} = (2r_1)\mathbf{x}^*, \quad T = T_{sea} + (T_1 - T_{sea})\,\theta^*,$$

where $\mathbf{x}^*$ represents the dimensionless coordinates and θ^* is a dimensionless temperature difference. Thence the problem becomes

$$\nabla^{*2}\theta^* = 0$$

in $x^{*2} + (y^* + h^* + 1/2)^2 > 1/4$ and $y < 0$ with boundary conditions $\theta^* = 1$ on $x^{*2} + (y^* + h^* + 1/2)^2 = 1/4$ and $\theta^* = 0$ on $y^* = 0$. Here $h^* = h/(2r_1)$.

This problem can be solved using a conformal mapping approach (Baddoo *et al.*, 2020). We set $z^* = x^* + iy^*$, where i is the imaginary number. Then a Möbius transform is used to map the half plane with the disc of radius $1/2$ centered at

$$z^* = -i(h^* + 1/2)$$

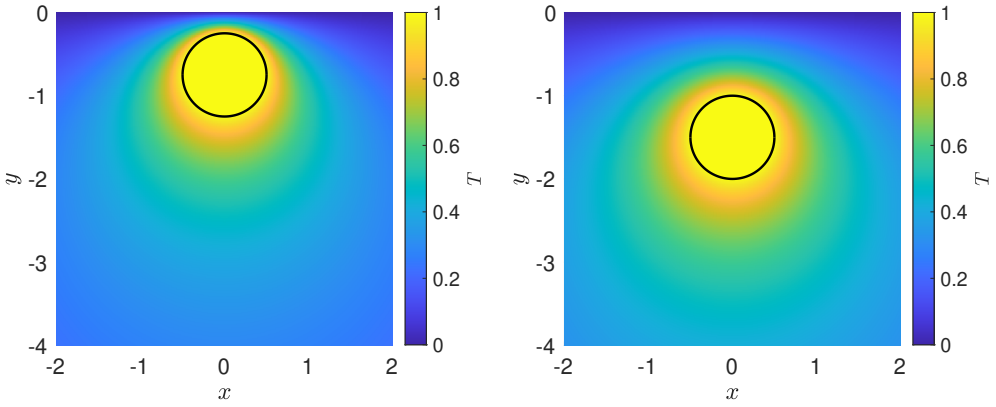


Figure 9: Dimensionless temperature profiles for a cable surrounded by a semi-infinite sediment extending to $y^* = 0$. The black circle shows the core of the cable. The cable is buried to a depth of $h^* = 0.25$ in (a) and $h^* = 1$ in (b).

removed, to an annulus. In this annulus, the heat equation admits a simple solution, which after applying the inverse transformation, yields the temperature profile

$$\theta^* = \mathrm{Re}\left[\frac{1}{\log\left(2h^* + \sqrt{4h^{*2}-1}\right)} \log\left(\frac{z^* - \frac{i}{2}\sqrt{4h^{*2}-1}}{z^* + \frac{i}{2}\sqrt{4h^{*2}-1}}\right)\right]$$

where Re is the real part of the expression in square brackets.

The dimensionless heat flux Q^* can be found from calculating $\partial\theta^*/\partial r^*$ on the boundary of the core $x^{*2} + (y^* + h^* + 1/2)^2 = 1/4$ and integrating over the surface. This gives

$$Q^* = \frac{4\pi}{\log\left(2h^* + \sqrt{4h^{*2}-1}\right)}$$

This can be redimensionalised to give the rate of heat generation in the core per unit length of cable

$$Q = k_o(T_1 - T_{sea})Q^*$$

where k_o is the thermal conductivity of the insulating layers and sediment. Hence the maximum (dimensional) temperature T_1 could be found by solving

$$I^2R(T_1) = \frac{4\pi k_o(T_1 - T_{sea})}{\log\left(2h/r_1 - \sqrt{4h^2/r_1^2 - 1}\right)}$$

for given h and I. In addition, the maximum burial depth h_{max} could be found for a specified maximum operating temperature T_{max} by solving for h with $T_1 = T_{max}$. Or the maximum current I_{max} could be found for a specified maximum operating temperature T_{max} by solving for I with $T_1 = T_{max}$.

3.9.1 Results

Sample profiles of the dimensionless temperature are shown in Fig. 9 for different burial depths and dimensionless fluxes are shown in Fig. 10.

Maximum burial depths in dimensional form are given in Fig. 11 assuming the sediment and insulating layers both have thermal conductivity $k_o = 0.3\,\mathrm{W\,K^{-1}\,m^{-1}}$. This value is an underestimate for the conductivity of the sediment and so this provides a conservative estimate for the maximum burial depth. To give an indication of the sensitivity to this value, the maximum burial depth is also given if both layers have conductivity $k_o = 0.6\,\mathrm{W\,K^{-1}\,m^{-1}}$. The maximum depth decreases rapidly as the electrical current increases. For a cable with a maximum operating temperature of $T_{max} = 70°\mathrm{C}$, the cable can be safely buried to depths of 1 m for electrical currents up to approximately 2100 A .

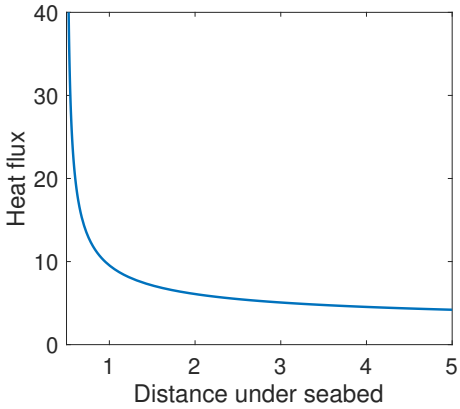


Figure 10: Dimensionless heat flux Q^* as a function of dimensionless burial depth h^*.

3.10 Summary and discussion

A considerable amount of work was conducted over the week of the MISG on various thermal effects that could potentially cause some problems to the high voltage cable. Models considered ranged from simple axi-symmetric heat transfer with averaged layer properties, a localised central heating and boundary conditions to examine different surface thermal properties of potential bio-matter, to full finite element solutions with some imagined, but realistic coating shapes. Models with multiple layers and ohmic heating of the interior were considered. Techniques employed included analytical solutions, complex function theory and full computational simulations. The thermal properties of cables, soil and biomatter obtained from the relevant literature were utilised in most calculations, but several worst-case scenarios, such as a cable buried in soil with low conductance, were also considered.

In spite of the variety of techniques employed and models used, this very thorough work provided a consistent set of results in terms of the implications for cable performance. It was found that given the properties of the cable

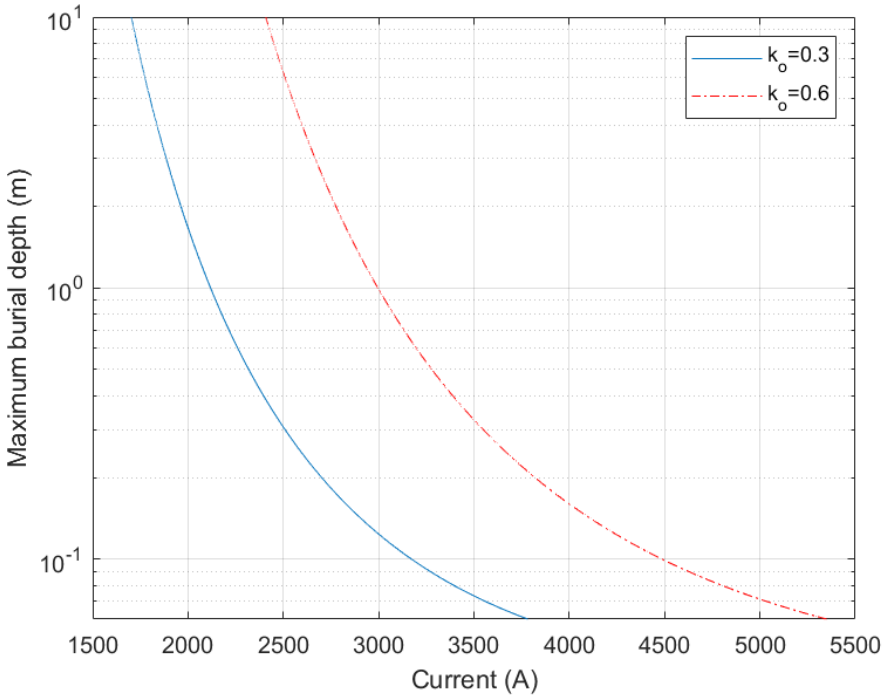


Figure 11: Maximum burial depth for the cable to remain within allowable operating temperatures as a function of the electrical current. The maximum operating temperature is $T_{max} = 70°C$. The seawater above the sediment has temperature $T_{sea} = 30°C$.The core of the cable is taken to have the same radius as the illustrative example in Fig. 2. The surrounding insulating layers are assumed to have the same thermal conductivity as the surrounding sediment, with both having $k_o = 0.3\,W\,K^{-1}\,m^{-1}$ (blue curve) or $k_o = 0.6\,W\,K^{-1}\,m^{-1}$ (red dash-dotted curve). The electrical resistance values are $R_{ref} = 7 \times 10^{-6}\,\Omega\,m^{-1}$ (the resistance at a reference temperature of 20°C) and $\beta = 2 \times 10^{-8}\,\Omega\,°C^{-1}\,m^{-1}$.

and the surrounding environment, the presence of layers of marine growth was unlikely to have serious implications for the internal heating of the cable, since the conductivity of the biomatter was sufficient to allow the heat to pass away from the surface of the cable at a sufficient rate to prevent overheating. Modelling results of the worst-case scenario of a completely buried cable also showed that the likelihood of decreased thermal performance was low. Although it is possible that we have missed some important factor that may impact thermal performance, we are reasonably confident of these results.

Finally, we note that two additional appendices are provided with further results. Appendix G gives semi-analytical expressions that could be applied for non-axisymmetric problems. Appendix H gives additional discussion related to all topics related to this chapter, but was received after the main report was completed.

4 Hydrodynamics

The previous section examined the possible deterioration of the cable performance due to heating effects. In this section, the effects of hydrodynamic forces on the cable, with a particular focus on the effects of biofouling, are considered. The marine growth has three key impacts that are relevant to the hydrodynamics: it can increase the effective radius of the cable, it may be non-axisymmetric, changing the effective shape of the cable, and finally it may alter the surface properties, which may increase the roughness.

A brief literature review and background to the problem is given in §4.1. The theory for laminar flow past a cylinder in two dimensions is discussed in §4.2 whilst unsteady flow is analysed in §4.3. CFD simulations are presented in §4.4. The possibility and dynamics of vortex-induced vibrations are investigated in §4.5.

4.1 Background

Friswell (1995) presented equations for analysing the steady flow past a three-dimensional underwater cable system. The analysis included towed systems, and the equations used to simulate the cable configuration are provided. To illustrate the solution of the resulting two-point boundary value problem using a shooting method, the example of a sea-to-buggy cable is investigated in De Zoysa (1978). The inclusion of cable lift is demonstrated through an example of a towed system that uses a stranded cable. Additionally, a simplified analysis of the cable tension's dependence on the cable length is presented. For various vehicle positions, the optimal cable length required to minimise the force on the vehicle ranges from three to six times the direct range of the vehicle from the ship.

Teng *et al.* (2022) investigated the hydrodynamic forces acting on small-diameter cables (with diameters ranging from 50 to 200 mm) under wave conditions. The investigation comprises 87 experimental tests covering a range of parameters, including $20 \leqslant K_C \leqslant 2000$, $10^4 \leqslant Re_p \leqslant 10^5$, $10 \leqslant \beta \leqslant 1000$, and $0.001 < k_s/D \leqslant 2.6$, where K_C refers to the Keulegan-Carpenter number (quantifying the relative magnitude of the wave oscillations), Re_p is the Reynolds number defined regarding the cable diameter and peak free stream velocity, β is the Stokes number, and k_s/D is the ratio between the seabed roughness and cable diameter. The results indicate that wave boundary layers have a significant impact on the forces acting on cables in contact with the seabed. The variation in force coefficients with governing parameters such as K_C and k_s/D is explained based on the characteristic features of the wave boundary layer, such as velocity deficit and wall turbulence. The force coefficients are influenced by two counteracting mechanisms: velocity reduction in the wave boundary layer decreases the force coefficients, while strong wall turbulence from the seabed increases them. Based on the findings, empirical formulae are proposed for evaluating the force coefficients of an on-bottom cable submerged in a wave boundary layer (cf. §4.3).

The presence of biofouling on submerged cables, such as electrical umbilical

power cables for floating wind turbines, can greatly impact their dynamic behaviour under wave and current conditions by increasing their size and mass. Therefore, it is crucial to quantify the impact of biofouling on the hydrodynamic coefficients, such as drag and inertia coefficients, of underwater power cables. To achieve this, experiments were conducted by Marty *et al.* (2021) in a flume tank using seven different configurations of cylinders colonised by marine growth, including realistic marine growth shapes and patterns with larger and sharper edges than those typically studied. The marine growth colonisation was reproduced through 3D printing covers based on statistical analysis of in situ observations and measurements. The tests were conducted under current conditions, horizontal oscillating motions, and the combination of both to simulate offshore wave and current conditions. The results indicated that the addition of oscillating motions had a significant impact on the calculated coefficients, with roughness leading to an increase in drag and inertia. Further studies are described in the thesis of Griffiths (2022), which examines the hydrodynamics and on-bottom stability of subsea cables.

One of the key questions posed during the study group was the extent to which marine growth alters the hydrodynamic forces on subsea cables. A desired output was a quantitative description that related quantities such as the thickness of growth and the current speed to the forces on the cable.

4.2 Laminar flow past a cylinder

It is reasonable to assume that the flow across the cable does not depend much on the along-cable direction, so that the flow can be treated as two-dimensional and perpendicular to the direction of the cable. In most cases, this greatly simplifies the analysis without compromising the results.

To obtain a basic understanding of the flow, it is a good starting point to analyse the idealised two-dimensional laminar flow past a circular cylinder. Other effects such as viscosity, shape changes and vorticity can be benchmarked against this base flow.

Therefore we assume the fluid is inviscid and incompressible and the flow is irrotational, so that the velocity, $\mathbf{u}$, may be written as

$$\mathbf{u} = \nabla\phi, \tag{25}$$

for a potential $\phi(x, y)$, that satisfies Laplace's equation in the fluid and $\nabla\phi \cdot \mathbf{n} = 0$ on the sea bed and the cylinder boundary where $\mathbf{n}$ is the normal to the surface (no flow through the surface of the cylinder). This problem is solved numerically using the lightning method of Gopal & Trefethen (2019) and an example of the results is shown in figure 12. The calculations reveal that the lift is negative and proportional to a^4/h^3, where a is the cylinder radius and h is its height above the sea bed. As expected, there is negligible lift on a cylinder far from the sea bed. These calculations do not include any circulation, which would modify the lift.

In the special case of a cylinder that touches the sea bed, an exact solution can be obtained with complex potential given by

$$W(z) = aU_0 \coth a\pi/z, \tag{26}$$

where a is the cylinder radius and U_0 is the far-field flow velocity. In this special case the lift is positive, which is associated with the larger flow velocity at the top boundary of the cylinder; see figure 12. The calculations were extended to elliptical cylinders, which may result from asymmetric marine growth; see figure 13. Again, we find negative lift unless the cylinder is in contact with the bed.

The cable can only move upwards if the lift exceeds its weight. The worst case is therefore when the cable is touching the base. However, even if the force is sufficient to move the cable upward, the lift immediately decreases so, for this model, we can assume the cable will remain stationary or at least very close to the floor if there is no change in the shape due to biofouling. If the cable is hanging freely then for a symmetric cable there is no lift using this ideal fluid model. It is therefore important to consider the effects of unsteadiness, different shapes and viscosity.

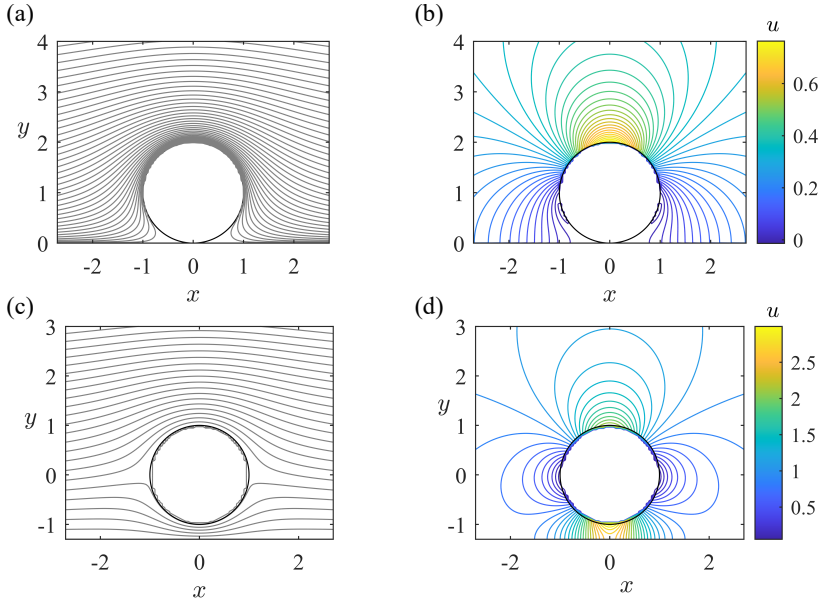


Figure 12: (a,b) Potential flow past a cylinder lying on the sea bed. (c,d) Potential flow past a cylinder elevated above the sea bed. The left-hand column shows the streamlines whilst the right-hand column shows the magnitude of the horizontal velocity, $\mathfrak{u}$.

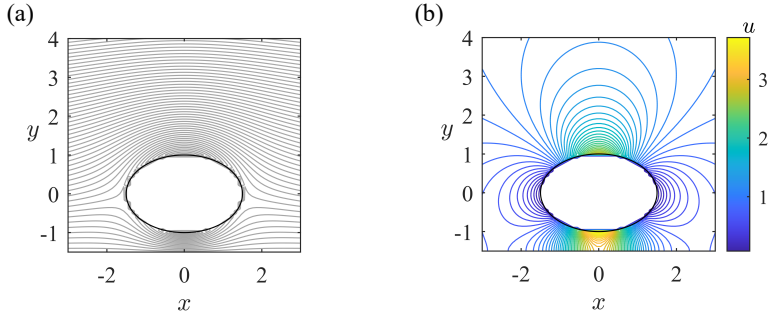


Figure 13: Potential flow past an ellipse showing (a) streamlines and (b) horizontal velocity.

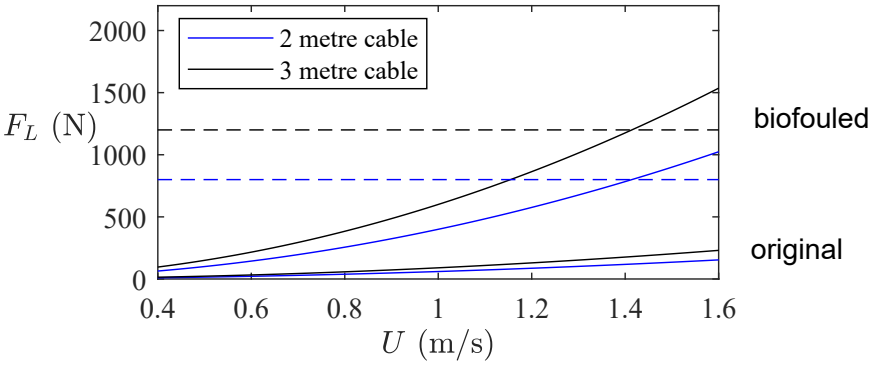


Figure 14: Lift on a free hanging cable of two or three metres length. Forces on the original (unfouled cable) and biofouled cable are calculated using (27). The dashed lines show the force needed to overcome the weight of the cable.

4.3 Unsteady flow

As discussed above, the Reynolds number for the flow lies in the range 10^4 to 10^5 and so it is likely that potential flow theory breaks down and does not completely describe the flow. At those Reynold's numbers the flow becomes unsteady, with vortices shed by the cylinder. As the speed of the flow increases these vortices may begin to oscillate (see section 4.5). The empirical law for the lift in this case is

$$F_L = \frac{1}{2}\rho_w C_L U^2 A, \tag{27}$$

where ρ_w is the density of water, U is the flow velocity, A is the area of cable facing the flow ($A = 2aL$), and C_L is the lift coefficient, which is determined empirically.

The original (unfouled) cable has radius $a = 0.1$ metres and lift coefficient of approximately $C_L \approx 0.3$. The (positive) lift force given by (27) on a free-hanging section of two or three metres of cable is plotted in figure 14 as a function of the flow velocity. The horizontal dashed lines represent the

net weight of the cable (40 kg/m) and so the lift on the original cable is insufficient to exceed the cable weight (cf. section 4.4).

However, marine growth can enhance the lift force due to both increased radius and increased lift coefficient associated with the roughness. As an example, consider the same two or three metre cable but for which the biofouling has doubled the radius to $a = 0.2m$ (say). In that case the lift coefficient becomes $C_L \approx 1$, and it may be possible for the lift to overcome the weight and drive the cable upwards at flow velocities above about $U > 1.4$ m/s; see figure 14.

Finally, we note that a similar empirical formula applies for the drag,

$$F_D = \frac{1}{2}\rho_w C_D U^2 A, \tag{28}$$

where C_D is the drag coefficient. Note that this may vary by a factor of up to 4 with the increased roughness associated with marine growth. The drag on the cable is in the range $100 - 400\ Nm^{-1}$ depending on the degree of biofouling (cf. section 4.4).

4.4 Computational Fluid Dynamics Modelling

If one wishes to consider all possible effects of concern, it is necessary to use a full computational model. This is called Computational Fluid Dynamics (CFD) and we applied it to this problem. Simulations were performed using a CFD solver in two-dimensions.[1]

Assuming the standard x, y reference frame with the axis of the infinite cylinder parallel to the x-direction we set the depth of the seabed to be 10m, the water density to 10^3 kg/m^3 and assume laminar (non-turbulent) flow with a left to right speed of $U = 1$m/s.

The results of the first case considered are shown in Figure 15, which shows the pressure field and velocity contours for the case of the cylinder detached

[1] https://apmr.matelys.com/BasicsMechanics/Fluid/FlowAroundADisk.html and https://demonstrations.wolfram.com/StreamlinesForLaminarFlowPastARotatingSolidCylinder

from the seabed. The center of the section of the pipe is fixed at a distance from the seabed equal to the diameter of the pipe (so the cylinder is one radius above the ocean floor). It is clear that there is a high pressure region at the bottom of the cylinder and a lower pressure field on the top and therefore we expect a net lift force acting on the cylinder.

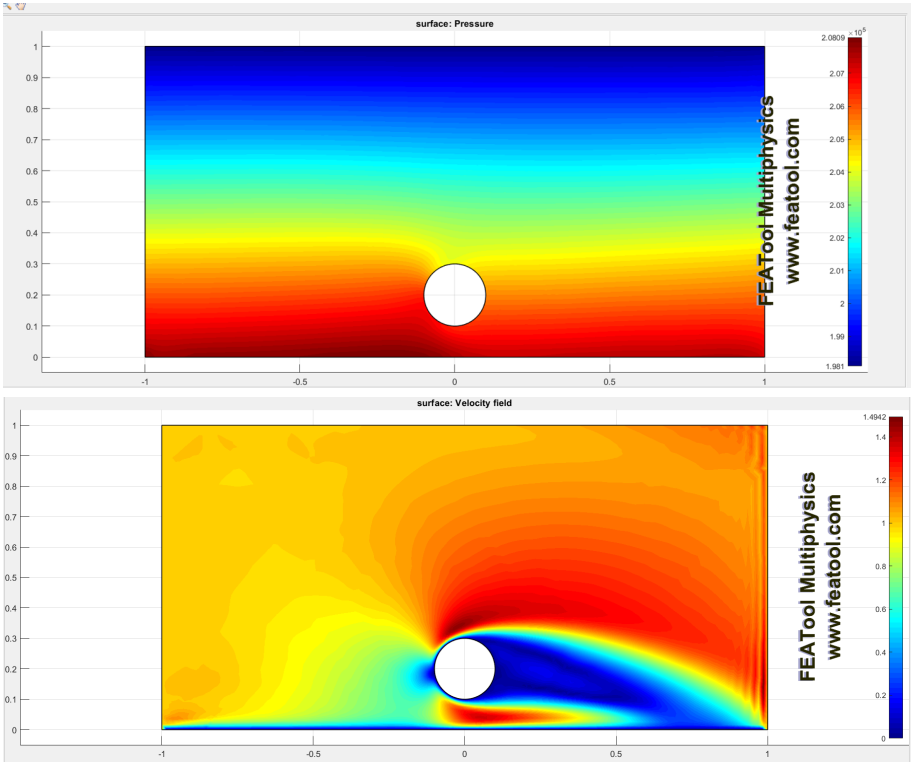


Figure 15: Pressure field (top) and velocity contours (bottom) around the cylinder for the case of the cable raised one cable radius above the ocean floor. Here the diameter, $\mathsf{D} = 20\text{cm}$, $\mathsf{U} = 1\text{m/s}$ and the cylinder is smooth with no biomatter attached.

Integrating the pressure and shear stress distribution over the cylinder contour

$$L = \oint_{\mathcal{C}} (-p n_z + \tau t_z) d\ell$$

we find a positive lift of 376 Nm^{-1}. We observe the lift per length is approximately half the weight of the cable per length and, as a result, we conclude this cable will not float in this configuration. The cylinder in its equilibrium configuration will lay on the seabed. The drag for this case was computed to be 155 Nm^{-1}.

In our second study, the flow past a cylinder resting on the seabed was simulated. An irregular surface was tested by adding sharp angles to the silhouette of the cylinder in order to mimic the presence of marine life attached to the cable. We show the pressure and velocity fields in Figure 16.

The drag force was obtained by integrating the pressure and shear stresses over the cable's lateral surface, according to the formula

$$D = \oint_{\mathcal{C}} (-p n_y + \tau t_y) d\ell \tag{29}$$

A value of 164 N/m was found for the drag per unit length. This is not significantly different from the result in the first study. In (29) p is the pressure, τ the shear stresses, n_y and t_y are respectively the y-component of the outward unit normal and the y-component of the tangent to the cylinder and $\mathcal{C}$ is the (irregular) contour of the cable with marine life attached.

Finally, we doubled the radius of the cable compared to the configuration in the second study and the results are shown in Figure 17).

A drag value of 299 Nm^{-1}, i.e. almost twice as much as in the second study, was found. Since the radius was doubled for this simulation, this is in agreement with the formula (28) for drag force, F_D, given above. These

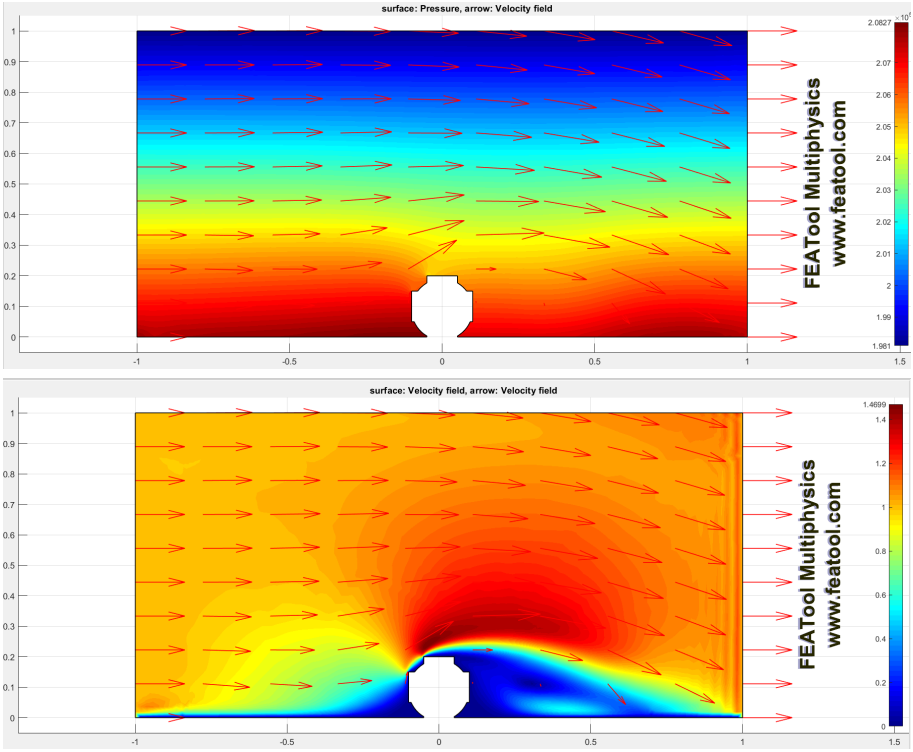


Figure 16: Pressure field (top) and velocity contours (bottom) for a cable sitting on the ocean floor. Arrows indicate local velocity. The cable diameter is $D = 20\text{cm}$ and the flow speed is $U = 1\text{m/s}$. The cylinder shape has been distorted to model some roughness due to marine growth.

calculations indicate that the changes in radius caused by biofouling may be a significant factor in changing the drag, and that the standard formulae for drag (28) and lift (27) can be used to give good estimates for these forces.

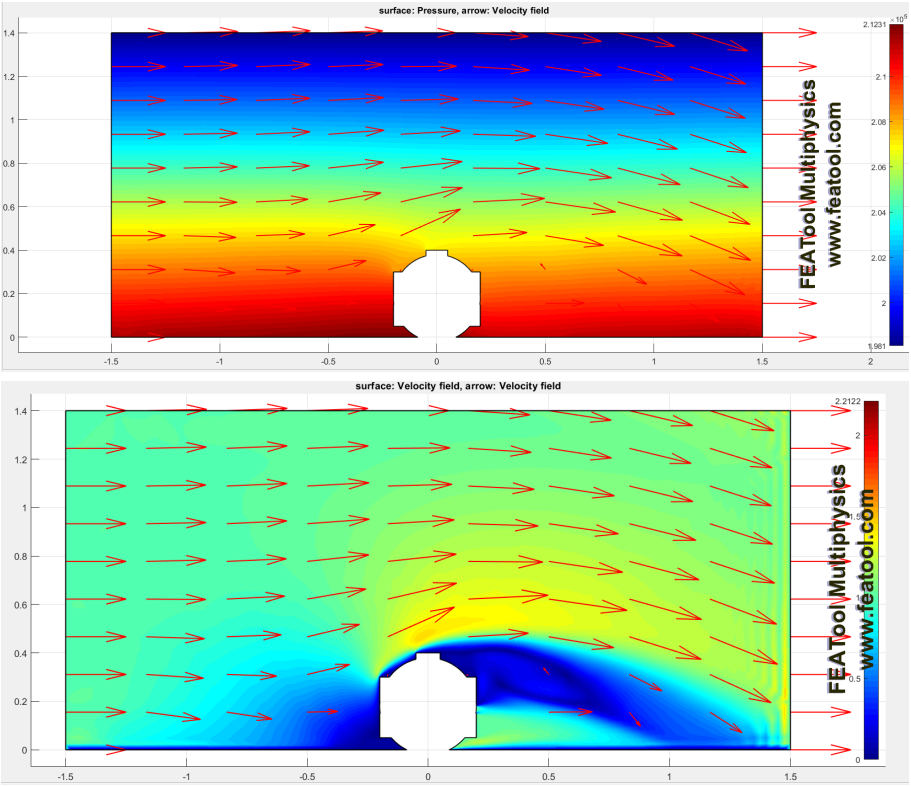


Figure 17: Pressure field (top) and velocity contours (bottom) for a cable sitting on the ocean floor with a mean flow of $U = 1$. Arrows indicate local velocity. The cylinder diameter has been increased to $D = 40$cm, and the cylinder shape has been distorted to model some roughness due to marine growth.

4.5 Vortex-induced vibration

A very common phenomenon arising from fluid-structure interactions that is very well known to engineers is Vortex Induced Vibrations (VIV). In this phenomenon the vortex shedding arising in the wake of flow past a bluff body gives rise to an oscillatory motion of the bluff body. This happens at higher

flow rates (see Section 4.3). A classical example of this can occur in the flow past a circular cylinder. When liquid passes over a cylinder, the viscosity causes the formation of a boundary layer on the surface. This layer eventually separates from the body leading to a train of vortices behind the cylinder. Under certain conditions, the vortex shedding gives rise to an oscillatory flow in which the vortices move up and down. As a consequence, the resulting lift and drag forces on the cylinder oscillate transverse to the flow, and to a lesser extent, inline to the flow. The motion of the cylinder acts like a feedback disturbance to the fluid and affects the formation of vortices. A wide range of literature, experimental, analyticl and numerical, is available on the this problem due to the ubiquity of the circular cylinder in real applications (see Williamson & Govardhan, 2004, for a review paper).

VIV is of relevance for deep sea freely spanning structures as stated in the opening paragraphs of Jin & Dong (2016), *"Pipelines are widely used in offshore and subsea engineering .... these pipelines can suffer from time varying stresses and fatigue damage resulting from the vortex induced vibrations(VIV). Therefore, determination of allowable freespan length plays a crucial role in design of offshore pipelines..."*.

4.6 Mathematical model

Due to the practical and theoretical importance of VIV, a large variety of models have been developed over the years that can be classified into three main types. These models mainly consider the simple case of 2D oscillations in the direction transverse to the cylinder. Moreover, the cylinder motion is simply modelled as an elastic oscillator with a spring and a damper attached, neglecting all of the nonlinearities in the cylinder's motion. These models are all phenomenological by nature i.e. they are based on some experimental results from fixed or forced oscillating cylinders, and all aim to predict the vibration of the free cylinders.

The final model described by Facchinetti *et al.* (2004) includes most of the

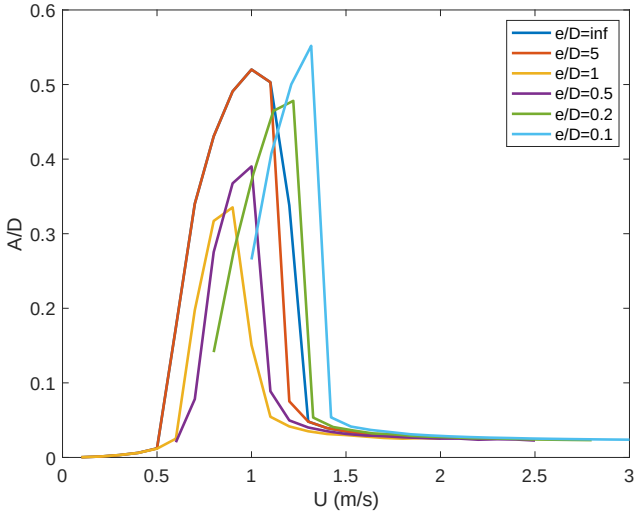


Figure 18: Amplitude response during VIV of a cable of length 2.5m as a function of cross-stream velocity U for different distance from the seabed. A is the amplitude of oscillations of the cable, D is the diameter of the cable and e is the distance between the bottom of the cable and the seabed.

evolution phases of wake oscillator models. They model the fluctuating vortex sheet due to a transverse oscillating cylinder with motion $y(t) = A\sin(2\pi f_e t)$ by a nonlinear self-excited oscillator satisfying the van der Pol equation,

$$\ddot{q} + \Omega_f \epsilon (q^2 - 1)\dot{q} + \Omega_f^2 q = \frac{A_c}{D}\ddot{y}(t) \tag{30}$$

where ϵ is a growth rate parameter governing the damping in the equation, D is the diameter of the cylinder, $q(t)$ is a dimensionless wake variable usually interpreted as the reduced vortex lift coefficient given by $q(t) = 2C_L(t)/C_L^0$ and $\Omega_f = 2\pi f_{vs_0}$ with f_{vs_0} the natural vortex shedding frequency of the fixed

cylinder. $C_L(t)$ is the time dependent lift coefficient, and C_L^0 is the lift if the cylinder is fixed. The forcing on the right hand side models the effects of the cylinder on the near wake dynamics where A_c represents the strength of the coupling between the cylinder and the wake. When $A_c = 0$ i.e. a fixed cylinder, the wake oscillator gives a stable quasi-harmonic solution of amplitude 2 at the angular frequency Ω_f matching the vortex shedding of a fixed cylinder.

Facchinetti *et al.* (2004) systematically studied the effect of cylinder motion on the wake dynamics by considering the forcing of the possible first-order forms $y, \dot{y}, \ddot{y}$ and found that $\ddot{y}$ matched the experimental data quite well. They determined the parameters α and ϵ based on the experimental results with forced system models leading to $\epsilon = 0.3$ and $A_c = 12$ to be a good match.

In a preliminary analysis relevant to the Sun Cable project, the model of Jin & Dong (2016), which is a modification of the wake-oscillator model of Facchinetti *et al.* (2004), was used in the presence of a bottom planar wall. In this model the cylinder motion is not prescribed and is allowed to evolve freely.

The response of a cylinder of diameter D is modelled as a spring-mass-damper system forced by the wake variable q as follows

$$m_e\ddot{y} + (c + \gamma\rho D^2\Omega_f)\dot{y} + ky = \frac{1}{4}\rho U^2 D C_{L0} q, \tag{31}$$

while the wake-oscillator model is modified to the following form,

$$\ddot{q} + \epsilon\Omega_f(q^2 - 1)\dot{q} + \Omega_f^2 q + \alpha f_n \Omega_f q^2 = \beta\frac{A_c}{D}\ddot{y}(t) \tag{32}$$

which has two more parameters associated with the fourth and fifth terms, α and β. We refer the reader to section 2 of Jin & Dong (2016) for more details on the parameters in this model.

4.7 Sample calculations of vortex induced oscillations

To get an estimate of the typical amplitudes of VIV experienced by Sun Cable's cable as a function of the speed of the ocean current, we simulated Eqs. (31) and (32) for different values of gap ratio e/D where e is the distance from the bottom of the cylinder to the planar wall. The results are shown in Fig. 18.

We found that for a range of ocean current velocity $0.5 \lesssim U \lesssim 1.5$, there may be a resonance between the natural frequency of oscillation of the cylinder and the vortex shedding frequency that results in a relatively large amplitude response. However, even in this state of resonance, the maximum amplitude of oscillations of the cable is only of the order of the radius of the cable. This preliminary analysis suggests that the deformations are not of sufficient magnitude to cause serious problems unless they are sustained for a significant period of time leading to fatigue. The VIV characteristics of the cable may change with marine growth wrapped around it and some further related work can be seen in Kurian *et al.* (2017) and Xu *et al.* (2022).

5 Summary

The group was able to consider a number of possible factors that might affect the efficient performance of the cable. Cables in a subsea location for an extended period of time can gather considerable biomatter on the exterior. The nature and extent of this will depend on depth and ocean conditions such as light, temperature and salinity. However there is limited data available from which to make predictive statements on the likely extent of marine growth.

Calculation of thermal factors indicate that the most serious effects are likely to be on a cable buried in sand, as this will provide a complete covering to some depth, maximising the heat retention. However, even in this situation, preliminary calculations indicate it would be unlikely to cause serious overheating. Calculations of the hydrodynamic forces indicate that they are not

sufficient to cause direct damage to the cable except in cases where the cable becomes snagged and then exhibits a rocking back and forth over an extended period of time, thus wearing away at the covering. A full analysis of this requires further information about the cable construction.

A considerable amount of work was conducted during the week of the study group examining each of the questions posed. Preliminary calculations indicate that none of the factors would be sufficient to cause significant damage or performance deterioration in the cable, except perhaps over an extended period of time. This is a subject requiring further investigation.

A Thermal performance appendices

B Value of the heat transfer coefficient

The value of the heat transfer coefficient $\alpha \approx 200\,\mathrm{W\,K^{-1}\,m^{-2}}$ used in the main report assumes natural convection and a smaller diameter than that of an actual power cable. Thus it is likely an underestimate of the actual value. Here we provide some further discussion of its value, although note that provided it is "large" the main results presented in this report are minimally affected.

For over 95% of the length of the cable, the lower-quartile water currents are above $0.01\,\mathrm{m\,s^{-1}}$ giving Reynolds numbers above 1000, while for over 50% of the cable, the lower-quartile water currents are above $0.1\,\mathrm{m\,s^{-1}}$ giving Reynolds numbers above 10^4. Thus some forced convection occurs, and more accurate values of α for a given location could be obtained using well-established empirical relations for forced convection (e.g., see Incropera *et al.*, 1996). Here we discuss the range of values using empirical relationships between the Nusselt number (nondimensional heat transfer coefficient) and Reynolds number (nondimensional fluid velocity) for forced, rather than natural convection. An example is the formula used by McAdams (1954) (see

also Perkins Jr & Leppert, 1962; Fand, 1965):

$$\mathrm{Nu} = (0.35 + 0.56\mathrm{Re}^{0.52})\mathrm{Pr}^{0.3}. \tag{33}$$

Here Pr is the Prandtl number, which is the ratio of thermal to momentum diffusivity. For ocean water at the temperatures considered, $\mathrm{Pr} \approx 10$. In terms of our parameters, the Reynolds and Nusselt numbers are

$$\mathrm{Re} = \frac{UD}{\nu}, \qquad \mathrm{Nu} = \frac{\alpha D}{k_w}.$$

Here U is the far-field fluid velocity, $D = 2r_n$ is the diameter of the cable, ν is the kinematic viscosity and k_w is the thermal conductivity of the water. For Reynolds numbers $1000 < \mathrm{Re} < 10^4$, (33) gives

$$41 < \mathrm{Nu} < 135.$$

Using the conductivity of ocean water $k_w \approx 0.6\,\mathrm{W\,K^{-1}\,m^{-1}}$ and radius $r_n = 0.08\,\mathrm{m}$, the range of heat transfer coefficients α is thus

$$155 < \alpha < 506 \qquad (\mathrm{W\,K^{-1}\,m^{-2}}).$$

C An alternative solution method for §§3.5.1

As we are assuming steady state and that there is no heat generated in the insulating layers outside the copper core, the total heat flux per unit length through any cylindrical shell of radius $r \geqslant r_1$ must be Q. This can also be expressed via Fick's law as $-2\pi r k_{i+1} dT/dr$ for $r_i \leqslant r \leqslant r_{i+1}$. Hence

$$Q = 2\pi r \left(-k_{i+1}\frac{dT}{dr}\right). \tag{34}$$

Let $T = T_i$ at $r = r_i$. Solving (34), the temperature distribution is then

$$T - T_i = \frac{Q}{2\pi}\frac{\log(r_i/r)}{k_{i+1}} \tag{35}$$

and the temperature difference between the inner and outer interface of each shell is

$$T_i - T_{i+1} = \frac{Q}{2\pi} \frac{\log(r_{i+1}/r_i)}{k_{i+1}}. \tag{36}$$

At the outer boundary, balancing heat generation with convective heat transfer to the surrounding water gives

$$Q = 2\pi r_n \alpha (T_n - T_{sea}), \tag{37}$$

where r_n is the outer radius, α is the convective heat transfer coefficient and T_{sea} is the marine water temperature. Combining these expressions, the temperature difference between the core-insulation boundary and the water is

$$T_1 - T_{sea} = \frac{Q}{2\pi k_e}, \tag{38}$$

equivalent to (10).

D Temperature distribution in a conducting core

Here we present a more complete calculation of the temperature profile in the cable carefully taking into account the temperature dependence in the core.

Consider a straight cylindrical cable of total length L (m). It contains a solid copper core of radius r_1 (m) carrying electrical current and covered by $n-1$ uniform layers of coaxial insulation. The thermal conductivity of copper is k_1 ($W\,K^{-1}\,m^{-1}$). The total power of Joule heating in the conducting core is Q, which is dissipated through insulation. Individual insulation layers have thermal conductivities k_i ($W\,K^{-1}\,m^{-1}$) and outer radii r_i (m), $i = 2, 3, \ldots, n$.

Our task is to derive the expression for the temperature distribution and the total heat production power in the central conducting (copper) core of the cable. Let U be the electric potential difference applied to the conducting

core of length L. Since the core is electrically insulated, the value of the electric potential must be constant in any cable cross-section perpendicular to its axis. On the other hand, if the temperature of the core is not constant in the radial direction, then the electrical conductivity of the core material and thus the density of the electrical current will vary radially. In turn, this will result in variable heat production across the cable core.

Consider a thin cylindrical shell within the electrically conductive core of the cable of radius $r < r_1$ and thickness Δr. The electrical resistance of this shell is

$$\rho = \frac{\rho_{ref} L}{2\pi r \Delta r}[1 + \alpha_\rho (T_1(r) - T_{ref})] = \frac{\rho_{ref} L}{2\pi r \Delta r}[1 + \beta(\Theta(r) - 1)]\,, \qquad (39)$$

where ρ_{ref} ($\Omega{\cdot}m^2/m$) is the resistivity of copper at the reference temperature T_{ref}, α_ρ (1/K) is its temperature coefficient, $\Theta(r) = T(r)/T_{ref}$ is the non-dimensional temperature and $\beta = \alpha_\rho T_{ref}$. The power of heat generation ΔP (W) in this shell is

$$\Delta P = \frac{U^2}{\rho} = \frac{2\pi r \Delta r U^2}{\rho_{ref} L[1 + \beta(\Theta(r) - 1)]} \approx \frac{2\pi r \Delta r U^2}{\rho_{ref} L}(1 + \beta - \beta\Theta(r))\,, \qquad (40)$$

where the fact that $\beta \ll 1$ for copper is used to linearise and obtain the final expression.

Since this heat can only be dissipated through the surface of the cable, the thermal energy balance equation written for a cylindrical shell takes the form

$$-2\pi(r + \Delta r) L k_1 \left.\frac{dT}{dr}\right|_{r+\Delta r} + 2\pi r L k_1 \left.\frac{dT}{dr}\right|_{r} = \Delta P\,. \qquad (41)$$

Upon rescaling $r \to r_1 r$ so that from now on r denotes the non-dimensional radius and taking the limit $\Delta r \to 0$ this leads to a differential equation describing the balance between Joule heating and the outward heat flux

$$\frac{k_1 L T_{ref}}{r_1} \frac{d}{dr}\left(r \frac{d\Theta}{dr}\right) = -\frac{r_1 r U^2}{\rho_{ref} L}(1 + \beta - \beta\Theta(r))\,, \qquad (42)$$

which we rewrite as

$$\Theta'' + \frac{\Theta'}{r} - Q_2\Theta = -Q_1\,, \tag{43}$$

where

$$Q_1 = S(1+\beta)\,, \quad Q_2 = \beta S\,, \quad S = \frac{U^2}{\rho_{ref} T_{ref} k_1}\frac{r_1^2}{L^2}\,. \tag{44}$$

Equation (43) is recognised as non-homogeneous modified Bessel's equation. The solution that is non-singular at the axis of the cable at $r = 0$ is given in terms of a zero-order modified Bessel function of the first kind I_0 as

$$\Theta(r) = \frac{Q_1}{Q_2} + cI_0(\sqrt{Q_2}r) = \frac{1+\beta}{\beta} + cI_0(\sqrt{\beta S}r) \tag{45}$$

$$= \frac{1+\beta}{\beta} + c\sum_{m=0}^{\infty}\frac{(\beta S r^2)^m}{4^m (m!)^2} \tag{46}$$

$$= \frac{1+\beta}{\beta} + c\left(1 + \frac{\beta S}{4}r^2 + \frac{\beta^2 S^2}{64}r^4 + \cdots\right)\,, \tag{47}$$

where c is an arbitrary constant that will need to be specified from boundary conditions. Substituting this expression into (40) and integrating over the core radius, we obtain the expression for the total heating power Q

$$\begin{aligned} Q &\approx \frac{2\pi r_1^2 U^2}{\rho_{ref} L}\int_0^1 r(1+\beta-\beta\Theta(r))dr \\ &= -\frac{2\pi c r_1^2 U^2}{\rho_{ref} L S}\int_0^{\sqrt{\beta S}} r I_0(r)dr = -\frac{2\pi c r_1^2 U^2}{\rho_{ref} L}\sqrt{\frac{\beta}{S}}I_1(\sqrt{\beta S}) \\ &= -\frac{\pi c\beta r_1^2 U^2}{\rho_{ref} L}\left(1 + \frac{\beta S}{8} + \cdots\right) \approx -\pi c\beta S k_1 T_{ref} L\left(1 + \frac{\beta S}{8}\right)\,. \end{aligned} \tag{48}$$

We can then find the constant c through the condition (10), which is given in non-dimensional form as

$$\Theta_1 = \Theta_{sea} + \frac{Q}{2\pi k_e T_{ref}}\,.$$

Substituting for $\Theta_1 = \Theta(1)$ from (47) and for Q from (48), we have

$$\frac{1+\beta}{\beta} + c\left(1 + \frac{\beta S}{4} + \frac{\beta^2 S^2}{64}\right) \approx \Theta_{sea} - c\,\frac{k_1}{k_e}\frac{1}{2}L\beta S\left(1 + \frac{\beta S}{8}\right),$$

from whence

$$c \approx \Theta_{sea} - \frac{1+\beta}{\beta} + \frac{1}{4}S\left(1 + 2\frac{k_1}{k_e}\right) - \frac{1}{64}\beta S\left(16S\frac{k_1^2}{k_e^2} + 3S + 16(\Theta_{sea} - 1) + 4\frac{k_1}{k_e}(3S \tag{49}$$

to order β.

The above expressions are derived in terms of the parameter S, which is defined in terms of the electric potential difference between the ends of the cable. However, its value depends on a consumer load that may change throughout a day in a way that cannot be controlled by the electricity provider. Therefore, the quantity U may not be easy to determine in practice. A more convenient characteristic of the cable load that is more readily available to the electricity provider is the total current I flowing through the cable, which can be measured at the provider's end of the cable. Algebraically, it is given by

$$\begin{aligned} I = \frac{Q}{U} &\approx -\frac{\pi c \beta r_1^2 U}{\rho_{ref} L}\left(1 + \frac{\beta S}{8}\right) \\ &\approx \pi\left(1 + \beta - \beta\Theta_{sea} - \frac{\beta S}{4}\left(1 + 2\frac{k_1}{k_e}\right)\right) r_1\sqrt{\frac{T_{ref} k_1 S}{\rho_{ref}}}\left(1 + \frac{\beta S}{8}\right), \end{aligned} \tag{50}$$

where (44), (48) and (49) have been used. Inverting (50), we obtain an approximate expression for parameter S in terms of the full current I that now can be used to evaluate both the temperature distribution and the total heat generation within the cable

$$S \approx \frac{I^2 \rho_{ref}}{\pi^2 k_1 r_1^2 T_{ref}}\left[1 + 2\beta\left(\Theta_{sea} - 1 + \frac{I^2 \rho_{ref}(4/k_e + 1/k_1)}{8\pi^2 r_1^2 T_{ref}}\right)\right], \tag{51}$$

which now can be substituted into (47) together with (49) to compute the temperature distribution inside the cable core.

As follows from (47), (49) and (51), the temperature at the edge of the core (equivalently the maximum temperature in the insulating layers of the cable) follows that of the cable environment with the difference between the two growing quadratically with the current.

E MATLAB code for maximum cable temperature

The code given below produces a plot of the maximum insulator temperature as a function of the electrical current for the illustrative cable given in Fig. 2. Various other input parameters are set in the early parts of the code.

```
% Plots cable temperature for varying current
clear

%
   ====================================================

% Physical Parameter Inputs
%
   ====================================================


% Data provided by industrial partner
SectionName = {'Conductor', 'Conductor screen', '
   Insulation', 'Insulation screen',...
    'Water blocking tape', 'Metal sheath', 'Inner
       jacket', 'Bedding', 'Armour', ...
    'Serving'}';
```

```
SectionMaterial = {'Copper circular stranded,
   compacted, water blocked', ...
    'Extruded bonded semi conductive compound', '
      Cross Linked Polyethylene (XLPE)', ...
    'Extruded bonded semi conductive compound', '
      Semi-conducting water-swelling tape', ...
    'Lead', 'Polyethylene compound', 'Polypropylene
      yarn', ...
    'Galvanized steel wires filled with bitumen', '
      Polypropylene strings'}';
Radius = [30, 2, 26.5, 1, 1, 3.5, 3.5, 2, 6, 5.5]';
   %[mm]
ThermalConductivity = [395, 1, 0.285, 1, 1, 60, 0.4,
    0.11, 50, 0.11]'; %[(W/(K*m))]
MassDensity = [8920, 1100, 1100, 1100, 1100, 11340,
   950, 920, 5000, 920]'; %[kg/m^3]
SectionSpecificHeat = [0.385, 2.1, 2.1818, 2.1, 2.1,
    0.125, 2.5, 1.9259, 0.5067, 1.9259]'; %[kJ/(kg*K
   )]

% Current Range (vector of values)
PCurrentRange=0:50:4000; % Current [A]

% Resistance Data (linear) R=R1+(R2-R1)/(T2-T1) * (T
   -T1)
PResistT1=0.007*1e-3; % Resistance over 1m at T1 [
   Ohm/m]
PResistT2=0.008*1e-3; % Resistance over 1m at T2

% Reference temperatures for resistances [degC]
T1ref=20;
T2ref=70;
```

```
% Temperature Limit [degC]
Tlimit=70;

% Convective Heat Transfer Coefficient on outside of
    cable
hconv=200; % [(W/(K*m^2))]

% Water temperature [degC]
SeaTemperature=30;

%
   ========================================================

% Calculation and Plot Code (no inputs)
%
   ========================================================



% Resistance increase per degC
beta=(PResistT2-PResistT1)/(T2ref-T1ref);
PResistTdep=@(T) PResistT1+beta*(T-T1ref);

% Cumulative Radius in m
CumRadius=cumsum(Radius)*1e-3;

% Thermal resistances
ThermalRes_Cond=log(CumRadius(2:end)./CumRadius(1:
   end-1))./ThermalConductivity(2:end);
ThermalRes_Conv=1/(CumRadius(end)*hconv);
ThermalRes_Total=sum(ThermalRes_Cond)+
   ThermalRes_Conv;
```

```
% Calculate temperature difference for each current
   value
DeltaT=PCurrentRange.^2*(PResistT1+beta*(
   SeaTemperature-T1ref))*ThermalRes_Total ...
    ./(2*pi-PCurrentRange.^2*beta*ThermalRes_Total);

DeltaT_uncorr=PCurrentRange.^2*PResistT1*
   ThermalRes_Total/(2*pi);

% Maximum Current Allowed
CurrentMax=sqrt(2*pi*(Tlimit-SeaTemperature) ...
    /(PResistTdep(Tlimit)*ThermalRes_Total));
fprintf('Maximum current is %.0f A\n',CurrentMax);

% Plot results
figure
plot(PCurrentRange,SeaTemperature+DeltaT,'k-', ...
    PCurrentRange,SeaTemperature+DeltaT_uncorr,'r--'
       , ...
    PCurrentRange,Tlimit*ones(size(PCurrentRange)),'
       b--')

xlabel('Current (A)')
ylabel('Cable Core Temperature (degC)')

legend('T with temperature dependent R', ...
    ['T with constant R at ' num2str(T1ref) ' degC'
       ], ...
    'Limit Temperature', ...
    'Location','northwest')
```

F MATLAB code for the thickness of marine growth

The code given below produces a plot of the maximum thickness of a uniform, conduction-only marine growth layer as a function of the current for a given maximum operating temperature. The code is for the illustrative cable geometry given in Fig. 2 and various other input parameters are set in the early parts of the code.

```
% Finds the maximum thickness of coating allowed for
    a prescribed cable
% temperature, as the current varies
clear

%
   ========================================================

% Physical Parameter Inputs
%
   ========================================================



% Data provided by industrial partner
SectionName = {'Conductor', 'Conductor screen', '
   Insulation', 'Insulation screen',...
    'Water blocking tape', 'Metal sheath', 'Inner
       jacket', 'Bedding', 'Armour', ...
    'Serving'}';
SectionMaterial = {'Copper circular stranded,
   compacted, water blocked', ...
    'Extruded bonded semi conductive compound', '
       Cross Linked Polyethylene (XLPE)', ...
```

```
    'Extruded bonded semi conductive compound', '
      Semi-conducting water-swelling tape', ...
    'Lead', 'Polyethylene compound', 'Polypropylene
      yarn', ...
    'Galvanized steel wires filled with bitumen', '
      Polypropylene strings'}';
Radius = [30, 2, 26.5, 1, 1, 3.5, 3.5, 2, 6, 5.5]';
   %[mm]
ThermalConductivity = [395, 1, 0.285, 1, 1, 60, 0.4,
    0.11, 50, 0.11]'; %[(W/(K*m))]
MassDensity = [8920, 1100, 1100, 1100, 1100, 11340,
   950, 920, 5000, 920]'; %[kg/m^3]
SectionSpecificHeat = [0.385, 2.1, 2.1818, 2.1, 2.1,
    0.125, 2.5, 1.9259, 0.5067, 1.9259]'; %[kJ/(kg*K
   )]

% Current Range (vector of values)
PCurrentRange=1000:10:4000; % Current [A]

% Resistance Data (linear) R=R1+(R2-R1)/(T2-T1) * (T
   -T1)
PResistT1=0.007*1e-3; % Resistance over 1m at T1 [
   Ohm/m]
PResistT2=0.008*1e-3; % Resistance over 1m at T2

% Reference temperatures for resistances [degC]
T1ref=20;
T2ref=70;

% Temperature Limit [degC]
Tlimit=70;
```

```
% Convective Heat Transfer Coefficient on outside of
    cable
hconv=200; % [(W/(K*m^2))]

% Water temperature [degC]
SeaTemperature=25;

% Conductivity of deposited layer [W/mK]
ThermalConductivity_Layer=0.6;

%
   ========================================================

% Calculation and Plot Code (no inputs)
%
   ========================================================



% Resistance increase per degC
beta=(PResistT2-PResistT1)/(T2ref-T1ref);
PResistTdep=@(T) PResistT1+beta*(T-T1ref);

% Heat generated at limit temperature for each value
    of current
QGenRange=PCurrentRange.^2*PResistTdep(Tlimit);

% Cumulative Radius in m
CumRadius=cumsum(Radius)*1e-3;

% Thermal resistances for cable without deposits
ThermalRes_Cond=log(CumRadius(2:end)./CumRadius(1:
   end-1))./ThermalConductivity(2:end);
```

```
ThermalRes_Conv=1/(CumRadius(end)*hconv);
ThermalRes_Total=sum(ThermalRes_Cond)+
    ThermalRes_Conv;

% Shortcut formula for finding thickness of
    deposited layer
% Neglects the decrease in thermal resistance from
    convection due to the
% increased radius
MaxThickness_Shortcut=max(0,CumRadius(end)*(exp(
    ThermalConductivity_Layer.* ...
      (2*pi*(Tlimit-SeaTemperature)./QGenRange-
         ThermalRes_Total)) - 1));

% Full formula, use root finding
MaxThickness_Full=zeros(size(QGenRange));

% Thermal resistance from extra layer and convection
ThermalRes_Extra=@(r_ex) log(1+r_ex/CumRadius(end))/
    ThermalConductivity_Layer ...
      +1/((CumRadius(end)+r_ex)*hconv);

for m=1:length(PCurrentRange)
      % Target total thermal resistance
      ThermalRes_Target=2*pi*(Tlimit-SeaTemperature)/
         QGenRange(m);
      % Thermal resistance required from extra layer
         and convection
      ThermalRes_ExtraTarget=ThermalRes_Target-sum(
         ThermalRes_Cond);
      % If a negative thermal resistance is required,
         skip the calculation
      if ThermalRes_Target <= ThermalRes_Total
```

```
        continue;
    end
    % Root finding function
    ThermalRes_fz=@(r_ex) ThermalRes_Extra(r_ex)-
       ThermalRes_ExtraTarget;
    MaxThickness_Full(m)=fzero(ThermalRes_fz,
       MaxThickness_Shortcut(m));
end

% Plot results
figure
semilogy(PCurrentRange,MaxThickness_Full,'k-', ...
    PCurrentRange,MaxThickness_Shortcut,'r--')

xlabel('Current (A)')
ylabel('Maximum Coating Thickness (m)')
ylim([1e-3, 1e3])
legend('Full','Shortcut','Location','southwest')

% Relative Error
ThickErrRE=(MaxThickness_Shortcut-MaxThickness_Full)
   ./max(MaxThickness_Full,eps);
MaxRE=max(abs(ThickErrRE));

%legend('T with temperature dependent R', ...
%    ['T with constant R at ' num2str(T1ref) ' degC
   '], ...
%    'Limit Temperature', ...
%    'Location','northwest')
```

G An exact solution to a non-axisymmetric problem

The solution for the heat distribution in a circular cable presented in Section 3.5 assumed an axisymmetric cable and boundary conditions. However, it is possible to extend this to consider variations in the shape of the cable or of the boundary conditions. For example, it would be possible to model the effects of different conduction through the surface to represent different coatings of biomaterial in different locations. The extension still incorporates the Fourier techniques discussed in Section 3.5 but includes variations in the conditions at different angles around the cable.

Let the temperature in the insulation part of the power cable be $T = T(r, \theta)$ where we consider a cross section of a cylindrical power cable which contains two concentric circular regions, a circular core and an outer ring-shaped insulation. Polar coordinates are used with r for the radial dimension and θ for the angle around the cable. The power cable centre is situated at the origin of this coordinate system. Here r_1 denotes the radius of the core and r_n denotes the radius of the whole cable as in the main text. We consider the possibility of different boundary conditions, such those due to the presence of marine growth, soil, or water, at different locations around the surface of the cylindrical cable. Allowing for this variation in behaviour with different angles, θ, the steady heat equation becomes,

$$r^2 \frac{\partial^2 T}{\partial r^2} + r \frac{\partial T}{\partial r} + \frac{\partial^2 T}{\partial \theta^2} = 0 \tag{52}$$

for $r_1 \leqslant r \leqslant r_n$, with boundary conditions

$$\frac{\partial T}{\partial r} = Q(\theta) \text{ at } r = r_1, \tag{53}$$

$$\frac{\partial T}{\partial r} = \alpha T - H(\theta) \text{ at } r = r_n, \tag{54}$$

and a technical condition that the solution be periodic in the angle θ, i.e. that $T(\theta + 2\pi) = T(\theta)$. In particular the condition (54) allows for different conduction rates at different locations around the cylinder.

These boundary conditions allow offer significant flexibilty for how marine growth, for example, is distributed around the outside of the power cable. We may set the conduction at any location around the cable by writing

$$Q(\theta) = \sum_{l=0}^{\infty} [f_l \sin(l\theta) + g_l \cos(l\theta)], \tag{55}$$

$$H(\theta) = \sum_{l=0}^{\infty} [F_l \sin(l\theta) + G_l \cos(l\theta)] \tag{56}$$

as the Fourier series expansions of $Q(\theta)$ and $H(\theta)$. Here α, f_l, g_l, F_l, G_l for $l \geqslant 0$ are constants that are determined by the form of the surface conditions.

Standard methods in partial differential equation theory allow for the solution of problem (52)–(56) to be found as

$$T(r,\theta) = \sum_{l=1}^{\infty} [(A_l r^l + B_l r^{-l}) \sin(l\theta) + (C_l r^l + D_l r^{-l}) \cos(l\theta)] + \hat{c}_0 \log_e(r) + \hat{d}_0 \tag{57}$$

where

$$A_l = \frac{f_l + l B_l r_1^{-l-1}}{l r_1^{l-1}} \quad \text{for } l \geqslant 1, \tag{58}$$

$$B_l = \frac{(\alpha/l) f_l r_n^l r_1^{-l+1} - F_l - f_l r_n^{l-1} r_1^{-l+1}}{l r_1^{-2l} r_n^{l-1} - l r_n^{-l-1} - \alpha r_1^{-2l} R_i^l - \alpha r_n^{-l}} \quad \text{for } l \geqslant 1, \tag{59}$$

$$C_l = \frac{g_l + l D_l r_1^{-l-1}}{l r_1^{l-1}} \quad \text{for } l \geqslant 1, \tag{60}$$

$$D_l = \frac{(\alpha/l) g_l r_n^l r_1^{-l+1} - G_l - g_l r_n^{l-1} r_1^{-l+1}}{l r_1^{-2l} r_n^{l-1} - l r_n^{-l-1} - \alpha r_1^{-2l} R_i^l - \alpha r_n^{-l}} \quad \text{for } l \geqslant 1, \tag{61}$$

$$\hat{c}_0 = g_0 r_1, \tag{62}$$

and

$$\hat{d}_0 = \frac{g_0 r_1}{\alpha R_i} - g_0 r_1 \log_e(r_n) + \frac{G_0}{\alpha}. \tag{63}$$

In practice there is no necessity that the terms given by (55) and (56) be quite so complicated. Simple cases, such as some a case in which portion of the cable boundary is completely insulated from the surroundings, can be computed very accurately without the necessity to use these full series expansions. This possibility is left for future work.

H Further exploration of Chapter 3

This work was contributed after the main report was completed, but contains some useful additional results and references.

In existing large DC submarine power cables, currents may be as large as $I = 1800$ A (e.g. Worzik, 2009). Currents twice that size are envisioned for the near future (Gordonnat & Hunt, 2020). However there are safe temperature limits that must be respected. Firstly, the insulating bands are made of resilient materials such as cross-linked polyethylene (XLPE) that must not be overheated. Although the next generation of these materials is likely to operate safely up to 90 °C, the safe limit is currently 70 °C. Secondly there is an almost universally adopted European environmental standard that the temperature of the local sea bed should not be increased by more than 2 °C. These restrictions lead to the concept of ampacity, which is the maximum safe current I_s that could be maintained without the surrounding materials overheating. For a cable of length $\ell = 1000$ km and cross section area 12 cm^2, the power of Ohmic heating would then be $I^2\ell/\pi r_1^2\sigma_1 \approx 50$ MW, where σ_1 is the electrical conductivity. This dissipated energy, around 4% of the envisaged power supply of 1.2 GW, heats the environment, but it is often safely spread over a very large volume.

The temperature coefficients for increase of electrical resistivity and of thermal

resistivity of copper are respectively 4 $\times 10^{-3}/°C$ and $2\times\ 10^{-4}/°C$. These are small numbers but as temperature increases by 50 degrees, the electrical conductivity may increase by 20%. The power of Ohmic heating would increase by the same proportion. Since the power is proportional to I^2, I_s would decrease by a factor that is approximately $\sqrt{1-0.2}$, which means a decrease of around 10%.

Ampacity is usually estimated using finite element models of heat flow. However a safe upper bound to I_s can be obtained from the exactly solved linear heat transport model. I_s must increase with electrical conductivity which decreases with temperature. Therefore it is safe to assume the constant value of minimum conductivity σ_1 at T_s, the upper bound of temperature. In addition, I_s must be an increasing function of the heat transfer coefficient α. This transfer coefficient controls cooling by the environment, and it varies greatly from around 200 to 5000 $W/°Cm^2$. Therefore it is safe to assume the worst-case value at the lower end of the range for α. The exactly solvable linear model will also allow us to quantify the effects of varying relevant parameters such as α and environment temperature T_e. Sea water has thermal conductivity 0.6 W/m°C. Calcite shell typically has a higher thermal conductivity of 3 in SI units, so it would not block heat flow out of the cable. Wet ocean sediment has thermal conductivity 0.9 W/m°C so it provides no more barrier than does sea water. Red seaweed has thermal conductivity 0.3 W/m°C (Balingasa, 2007), comparable to that of sea water, and the excess resistance over water would provide a weaker thermal barrier than the interior insulators. The effect of encircling seaweed could be estimated by halving α.

At steady state,

$$k_1\nabla^2 T + q = 0; \quad 0 \leqslant r < r_1, \tag{64}$$

$$q = \mathcal{I}^2/\pi^2 r_1^4 \sigma_1. \tag{65}$$

The character of physical outcomes must be determined by dimensionless parameters that are independent of choice of units. Therefore we set up the model in terms of dimensionless scaled variables. Lengths are scaled so that $\bar{r} = r/r_0$. Define a normalised dimensionless temperature $\bar{\theta} = \frac{T-T_e}{T_s-T_e}$.

Note: It is convenient to normalise temperature by the maximum allowable range which is $T_s - T_e$. The solution for temperature involves a logarithmic term $\log \bar{r}$ which is zero at the first interface $\bar{r} = 1$. The simplified boundary condition $\bar{\theta} = 1.0$ then leads to considerably simplified algebra when calculating ampacity.

In dimensionless form, the steady axi-symmetric temperature satisfies the governing Poisson and Laplace equations:

$$\frac{1}{\bar{r}}\partial_{\bar{r}}[\bar{r}\bar{\theta}_{\bar{r}}] + \mu = 0, \quad 0 \leqslant \bar{r} < 1, \tag{66}$$

$$\frac{1}{\bar{r}}\partial_{\bar{r}}[\bar{r}\bar{\theta}_{\bar{r}}] = 0, \quad 1 \leqslant \bar{r} < \bar{r}_N, \tag{67}$$

where N is the number of layers and μ is the dimensionless heating parameter

$$\mu = \frac{I^2}{\pi^2 r_1^2 k_1 [T_s - T_e]\sigma_1}. \tag{68}$$

With $T_s = 70\,^\circ\mathrm{C}$ and $T_e = 20\,^\circ\mathrm{C}$, this is a small number, $\mu = 7.7 \times 10^{-4}$, showing that within metallic conductors, the high thermal conductivity could keep gradients close to zero. The solutions are of the form

$$\bar{\theta} = c_2 - \frac{1}{4}\mu\bar{r}^2; \quad 0 \leqslant \bar{r} < 1 = \bar{r}_1, \tag{69}$$

$$\bar{\theta} = c_{2j-1} - c_{2j}\log\bar{r}; \quad \bar{r}_{j-1} \leqslant \bar{r} < \bar{r}_j; \quad 2 \leqslant j \leqslant N. \tag{70}$$

The dimensionless positive constants c_j are to be determined from boundary conditions. As well as assuming a finite temperature at $R = 0$, we assume continuity of both temperature and heat flux at all interfaces. In order to obtain a unique solution to the forward boundary value problem, one more boundary condition must be imposed. The standard condition is the Robin boundary condition for Newton cooling at the outer boundary $r = r_{ext}$. However for the purposes of calculating ampacity it is simpler to impose the relevant condition $\bar{\theta}(1) = 1$ which is the maximum allowable temperature at

the beginning $\bar{r} = 1$ of the first insulating layer. Given a full specification of these boundary conditions, as well as numerical values of the system parameters, the solution is known to be unique. However, the parameters α and T_e are adjustable to represent various environmental conditions. From the solution to the boundary value problem, we can then read off $\theta(r_{ext})$ and deduce I_s in a relatively straightforward inverse problem. If the design parameters of the cable are fit for purpose, the solution will include a feasible temperature $T(r_{ext}) \leqslant T_e + 2\,^\circ\mathrm{C}$ as well as a suitably large current $I \leqslant I_s$.
The resistance of the system is dominated by the insulators; there is a negligible temperature change across the metals. Therefore in order to estimate the outer temperature, we consider a system consisting only of a sequence of the insulating shells in series. Calculations show that the temperature within each metal layer is practically uniform. For the purpose of calculating I_s, the metal layers may be neglected. By conservation of energy, the heat flux at $r = r_{ext}$ will be $-\frac{r_1}{r_{ext}} k_1 T_r(r_1)$. In terms of dimensionless variables, the Robin boundary condition reduces to

$$\bar{\theta}_{\bar{r}}(1) = \bar{\alpha}\bar{\theta}(\bar{r}_{ext}); \tag{71}$$

$$\bar{\alpha} = \alpha r_{ext}/k_1. \tag{72}$$

As a further simplification, different insulating layers at the same conductivity will be rearranged to a single thicker layer. In a linear geometry, the resistance of an assembly of resistors in series will be independent of the ordering. In an axisymmetric flow with dimensionless curvatures necessarily satisfying $r_1/r < 1$, and the conductivities of insulating layers being within the same order of magnitude, the error due to the rearrangement should be small. The insulating layers outside of the copper core are now specified as having thermal conductivities expressed as:

$$\begin{aligned}
k_2/k_1 &= 0.0025; \quad 1 \leqslant \bar{r} < 1.13, \\
k_3/k_1 &= 7.13 \times 10^{-5}; \quad 1.13 \leqslant \bar{r} < 2.017 \quad \text{(XLPE range)}, \\
k_4/k_1 &= 0.001, \quad 2.07 \leqslant \bar{r} < 2.12, \\
k_5/k_1 &= 2.75 \times 10^{-5}; \quad 2.12 \leqslant \bar{r} \leqslant 2.37 \quad \text{(polypropylene)}.
\end{aligned}$$

Out of 41.5 mm total insulation thickness, this configuration exactly covers the first 28.5 mm of insulation in the designed cable, wherein most of the temperature drop occurs. The remaining 13mm are accounted for by relocating inwards where curvature is still low. From the boundary conditions,

$$c_3 = 1, \tag{73}$$

$$c_2 = c_3 + \frac{\mu}{4} = 1 + \frac{\mu}{4}, \tag{74}$$

$$c_4 = \frac{k_1}{k_2}\frac{\mu}{2}, \tag{75}$$

$$c_{2j} = \frac{k_{j-1}}{k_j} c_{2j-2}; \quad (j = 3, 4, 5), \tag{76}$$

$$c_{2j-1} = c_{2j-2} + (c_{2j} - c_{2j-2}) \log \bar{r}_j; \quad (j = 3, 4, 5). \tag{77}$$

The first three of these are explicit and the recurrence relations have solutions

$$c_{2j} = \frac{k_1}{k_j}\frac{\mu}{2}, \quad (j = 3, 4, 5) \tag{78}$$

$$c_{2j-1} = 1 + \frac{\mu}{2} m_j; \quad (j = 3, 4, 5) \tag{79}$$

$$m_j = \left[\left(\frac{k_1}{k_3} - \frac{k_1}{k_2} \right) \log \bar{r}_2 + \cdots + \left(\frac{k_1}{k_j} - \frac{k_1}{k_{j-1}} \right) \log \bar{r}_{j-1} \right]. \tag{80}$$

Hence from (71),

$$\bar{\alpha} = \frac{\mu}{2} \frac{1}{c_9 - c_{10} \log \bar{r}_5} \tag{81}$$

$$= \frac{\mu}{2} \frac{1}{m_5 - \frac{k_1}{k_5} \log \bar{r}_5} \tag{82}$$

$$\Rightarrow \ \mu = \frac{2\bar{\alpha}}{1 - \bar{\alpha}[m_5 - \frac{k_1}{k_5} \log \bar{r}_5]}. \tag{83}$$

Hence from (68) and (72), we have an explicit expression for I_s in terms of system parameters,

$$I_s = \pi r_1 \sqrt{\mu k_1 (T_s - T_e) \sigma_1}, \tag{84}$$

provided the temperature T_e is predicted to be less than $T_e + 2\,°C$. Note that over the whole solution, $1 - \bar{\theta}(\bar{r})$ is proportional to μ which is proportional to $I_s^2/(T_s - T_e)$. Therefore it is easy to see how to reduce the effective safe temperature T_s if the predicted exterior boundary temperature should be too large. This would lead to a corresponding decrease in I_s. For example, Table 1 shows that when the cable is encircled by weed at large depth, external boundary temperature is $2.3\,°C$ above ambient. If the excess of $0.3\,°C$ were to be taken seriously, T_s would need to be reduced to $69.7\,°C$, with a consequent minuscule reduction of I_s by one Amp. In all practical cases, this was not necessary even with a very large current, validating that the proposed cable design satisfies safety constraints. Table 1 shows the results for ampacity I_s rounded down to two digits. Encircling seaweed, and therefore partial occlusion by seaweed, has little effect on the ampacity and the outer boundary temperature.

T_e (°C C)	α (W/°Cm^2)	I_s (A)	T_N (°C C)
30	100	3800	31.4
30	200	3900	30.7
20	100	4200	21.8
20	200	4300	20.9
5	100	4700	7.3
5	200	4700	6.2

Table 1: Ampacity I_s and outer boundary temperature T_N in clear water ($\alpha = 200$), in seaweed ($\alpha = 100$) in shallow tropical water ($T_e = 30$), shallow European water ($T_e = 20$) and deep water $T_e = 5$.

References

Baddoo, P. J., Kurt, M., Ayton, L. J. & Moored, K. W. 2020 Exact solutions for ground effect. *Journal of Fluid Mechanics* **891**, R2.

Balingasa, C. R. 2007 Physical and thermal properties of the red seaweed *(Kappaphycus spp.)*. Master's thesis, Philippines Univ at Los Banos.

Čiegis, R., Ilgevičius, A., Liess, H., Meilūnas, M. & Suboč, O. 2007 Numerical simulation of the heat conduction in electrical cables. *Mathematical modelling and analysis* **12** (4), 425–439.

De Zoysa, A. P. K. 1978 Steady-state analysis of undersea cables. *Ocean Engineering* **5** (3), 209–223.

Di Pietro, D. A. & Droniou, J. 2020 *The Hybrid High-Order Method for Polytopal Meshes: Design, Analysis, and Applications*, *Modeling, Simulation and Applications*, vol. 19. Springer International Publishing.

Emeana, C. J., Hughes, T. J., Dix, J. K., Gernon, T. M., Henstock, T. J., Thompson, C. E. L. & Pilgrim, J. A. 2016 The thermal regime around buried submarine high-voltage cables. *Geophysical Journal International* **206** (2), 1051–1064.

Facchinetti, M. L., de Langre, E. & Biolley, F. 2004 Coupling of structure and wake oscillators in vortex-induced vibrations. *Journal of Fluids and Structures* **19** (2), 123–140.

Fand, R. M. 1965 Heat transfer by forced convection from a cylinder to water in crossflow. *International Journal of Heat and Mass Transfer* **8**, 995–1010.

Forteath, G. N. R., Picken, B., Ralph, R. & Williams, J. 1982 Marine growth studies on the North Sea oil platform Montrose Alpha. *Marine Ecology Progress Series* **8**, 61–68.

Friswell, M. I. 1995 Steady-state analysis of underwater cables. *Journal of Waterway, Port, Coastal, and Ocean Engineering* **121** (2), 98–104.

Gopal, A. & Trefethen, L. N. 2019 New Laplace and Helmholtz solvers. *Proceedings of the National Academy of Sciences* **116** (21), 10223–10225.

Gordonnat, J. & Hunt, J. 2020 Subsea cable key challenges of an intercontinental power link: case study of Australia–Singapore interconnector. *Energy Transitions* **4**, 169–188.

Griffiths, T. 2022 Hydrodynamics and on-bottom stability of subsea cables and small diameter pipelines. PhD thesis, The University of Western Australia.

Incropera, F. P., DeWitt, D. P., Bergman, T. L., Lavine, A. S. & others 1996 *Fundamentals of heat and mass transfer*, , vol. 6. Wiley New York.

Iswadi, A., Porter, J. S., Bell, M. C., Garniati, L., Harris, R. E. & Priyotomo, G. 2022 Establishing an agenda for biofouling research for the development of the marine renewable energy industry in indonesia. *Journal of Marine Science and Engineering* **10** (3), 384.

Jin, Yiming & Dong, Ping 2016 A novel wake oscillator model for simulation of cross-flow vortex induced vibrations of a circular cylinder close to a plane boundary. *Ocean Engineering* **117**, 57–62.

Kurian, V. J., Al-Yacouby, A. M. & Khir, A. R. M. 2017 Vortex-induced vibration tests of a marine growth wrapped cylinder at subcritical Reynolds number. *MATEC Web Conference* **103**, 02018.

Maksassi, Z., Garnier, B., Ould El Moctar, A., Schoefs, F. & Schaeffer, E. 2022 Thermal characterization and thermal effect assessment of biofouling around a dynamic submarine electrical cable. *Energies* **15** (9), 3087.

Marty, A., Berhault, C., Damblans, G., Facq, J-V., Gaurier, B., Germain, G., Soulard, T. & Schoefs, F. 2021 Experimental study of hard marine growth effect on the hydrodynamical behaviour of a submarine cable. *Applied Ocean Research* **114**, 102810.

McAdams, W. H. 1954 *Heat transmission*, 3rd edn. McGraw-Hill Book Company, Inc. New York, NY.

Perkins Jr, H. C. & Leppert, G. 1962 Forced convection heat transfer from a uniformly heated cylinder. *Journal of Heat Transfer* **84**, 257–261.

Schoefs, F. & Ameryoun, H. 2013 Probabilistic modeling of the biocolonization effects on hydrodynamic forces with several combinations of sea-state condition: a study on jacket-platforms in the Gulf of Guinea. In *International Conference on Offshore Mechanics and Arctic Engineering*, , vol. 55317, p. V001T01A056. American Society of Mechanical Engineers.

Scott, P. J. B. 1991 Rapid destruction of PVC piping by boring bivalves. *International Biodeterioration* **27** (1), 87–92.

Sherwood, J., Chidgey, S., Crockett, P., Gwyther, D., Ho, P., Stewart, S., Strong, D., Whitely, B. & Williams, A. 2016 Installation and operational effects of a HVDC submarine cable in a continental shelf setting: Bass strait, Australia. *Journal of Ocean Engineering and Science* **1** (4), 337–353.

Teng, Y., Griffiths, T., An, H., Draper, S., Tang, G., Mohr, H., White, D. J., Fogliani, A. & Cheng, L. 2022 Hydrodynamic forces on subsea cables immersed in wave boundary layers. *Coastal Engineering* **174**, 104101.

Tummers, M. J. & Steunebrink, M. 2019 Effect of surface roughness on heat transfer in Rayleigh-Bénard convection. *International Journal of Heat and Mass Transfer* **139**, 1056–1064.

Vinagre, P. A., Simas, T., Cruz, E., Pinori, E. & Svenson, J. 2020 Marine biofouling: A European database for the marine renewable energy sector. *Journal of Marine Science and Engineering* **8** (7), 495.

Williamson, C. H. K. & Govardhan, R. 2004 Vortex-induced vibrations. *Annual Review of Fluid Mechanics* **36** (1), 413–455.

Worzik, T. A. 2009 *Submarine Power Cables*. Springer, New York.

Xu, H., Wang, J., Li, Z., Liu, K., Yu, J. & Zhou, B. 2022 A study on the vortex induced vibration of a cylindrical structure with surface bulges. *Journal of Marine Science and Engineering* **10** (11).

Yemm, L. 2023*a* A new approach to handle curved meshes in the hybrid high-order method. *Accepted by Foundations of Computational Mathematics* .

Yemm, L. 2023*b* Polymesh. https://github.com/liamyemm/polymesh.

Author addresses

1. **Anja Slim**, School of Mathematics, Monash University, Australia.
mailto:anja.slim@monash.edu
orcid:0000-0002-6165-787X

2. **Edward Hinton**, School of Mathematics, University of Melbourne, Victoria, Australia.
mailto:edward.hinton@unimelb.edu.au
orcid:0000-0002-2204-1204

3. **Graeme Hocking**, Mathematics and Statistics, Murdoch University, Western Australia, Australia.
mailto:g.hocking@murdoch.edu.au
orcid:0000-0002-5812-6015

4. **Sami Al-Izzi**, School of Mathematics Statistics, University of New South Wales, Australia
mailto:s.al-izzi@unsw.edu.au

5. **Nitay Ben-Shachar**, California Institute of Technology, Pasadena, California, USA
mailto:nshachar@caltech.edu
orcid:0009-0002-2989-2295

6. **Phil Broadbridge**, La Trobe University, Melbourne, Vic, Australia

mailto:P.Broadbridge@latrobe.edu.au
orcid:0000-0003-1784-5344

7. **Pierluigi Cesana**, University of Kyushu, Fukuoka, Japan
mailto:pcesana81@gmail.com
orcid:0000-0002-0304-9382

8. **Michael Dallaston**, School of Mathematical Sciences, Queensland University of Technology, Qld, Australia
mailto:michael.dallaston@qut.edu.au
orcid:0000-0001-8993-6961

9. **Daniel Hayes**, Swinburne University of Technology, Hawthorn, Victoria, Australia
mailto:dthayes83@gmail.com
orcid:0000-0002-5656-6965

10. **Edoardo Fabbrini**, Univ. Grenoble Alpes, Inria, CNRS, Grenoble INP, Institute of Engineering, LJK, 38000 Grenoble, France
mailto:edoardo.fabbrini@inria.fr
orcid:0009-0005-1475-254X

11. **Chathranee Jayathilake**, School of Mathematics, Monash University, Australia.
mailto:Chathranee.AththanapolaArachchilage@monash.edu
orcid:0000-0003-4732-5665

12. **Benjamin Lee**, School of Mathematics, Monash University, Australia.
mailto:benjamin.lee2@monash.edu
orcid:0000-0001-7130-8393

13. **Melanie Roberts**, School of Environmental Science, Griffith University: Gold Coast, Queensland, Australia
mailto:m.roberts2@griffith.edu.au
orcid:0000-0003-4027-9651

14. **Cal Robertson**, School of Mathematics, Monash University,

Australia.
mailto:Calum.Robertson@monash.edu
orcid:0009-0000-1049-4014

15. **Jia Jia Qian**, School of Mathematics, Monash University, Australia.
mailto:jiajia.qian1@monash.edu
orcid:0000-0003-2184-490X

16. **Sergey Suslov**, Swinburne University of Technology: Hawthorn, Victoria, Australia
mailto:ssuslov@swin.edu.au
orcid:0000-0002-0998-2712

17. **Rahil Valani**, Department of Physcis, University of Oxford, Oxford, UK
mailto:rahil.valani@physics.ox.ac.uk
orcid:0000-0001-8346-0739

18. **Liam Yemm**, School of Mathematics, Monash University, Australia.
mailto:liam.yemm@monash.edu
orcid:0000-0003-2120-4048

19. **Wu Yunpei**, University of Kyushu, Fukuoka, Japan
mailto:wu.yunpei.258@s.kyushu-u.ac.jp
orcid:0009-0000-1168-9075